12-6-2018

Mechanical and tribological investigation of thin film coatings onto flexible polymeric substrate

Andrea Coelho Vincent

Recommended Citation

MECHANICAL AND TRIBOLOGICAL INVESTIGATION OF THIN FILM
COATINGS ONTO FLEXIBLE POLYMERIC SUBSTRATE

by

Andrea C. Vincent

A Thesis

Submitted in Partial Fulfilment of the

Requirements for the Degree of

Master of Science

Major: Physics

The University of Memphis

December 2018

© Andrea C. Vincent

To Emilia

Acknowledgements

First, thank you to my advisor, Dr. Firouzeh Sabri, for your support, guidance, and encouragement through my graduate career, and for being an inspiring example of personal and professional achievement to me. Your positive enthusiasm kept me going when I thought I may not be able to carry on. Thank you for believing in me even when I didn't.

Thank you to the professors and staff at the Department of Physics and Materials Science for always being available to assist and going above and beyond your duties to create a supportive educational environment.

Thank you to my graduate and undergraduate friends and lab mates for sharing with me in this adventure. I can't overstate how important our time together has been, whether it was collaborating in studies, discussing personal troubles, or celebrating victories. I will treasure it all for the rest of my life.

Thank you to my parents for loving me unconditionally and supporting my dreams, for always being there for me and encouraging me to reach for the stars. I would not be the person I am today without your example of dedication and perseverance.

Most of all, thank you to my husband, John, for being my partner, for having my back no matter what, for being a wonderful father to our daughter, and for always pushing me to reach my potential. I couldn't have done it without you.

Abstract

Elastomers of the polydimethylsiloxane family are paramount to science and engineering due to their useful properties. Much work has gone into characterizing these polymers to optimize their performance. However, at this time there is little published literature dedicated to understanding and controlling its frictional behavior.

In this study, Sylgard was characterized as a function of crosslinker ratio and curing temperature, then coated with Silastic using two different techniques resulting in a bilayer. The bilayer was characterized both in bulk and surface properties, and those results compared between techniques and uncoated Sylgard.

It was demonstrated that spin coating can produce a well-bonded topcoat that possesses significantly lower frictional force than that of Sylgard alone at ambient and cryogenic temperatures. Changes in other properties were also quantified. This technique of PDMS surface modification may reduce the need of lubricants in mobile joints and extend component lifetime by shielding it from friction wear.

Contents

List of Tables

List of Figures

1. Introduction

Siloxane-based polymers

Polydimethylsiloxane (PDMS) is a highly versatile siloxane-based elastomer (Figure 1) which has unique bulk and surface properties that have made this class of materials of great importance to many industries [1-6]. Some of the materials from this family are thermosetting, transparent in the visible range, and thermally and electrically insulating. Once it is fully cured, the connection between polymer chains is irreversible and as a result maintains its properties (for the most part) despite chemical and thermal treatments [13]. Among the different types of PDMS available, Sylgard® 184 is one of the most studied formulations and has been used extensively in a variety of applications and industries [6].
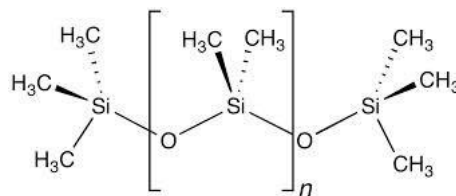
Figure 1: PDMS molecular diagram [55].

For example, Ziaie et al. [1] described fabrication techniques for creating MEMS (microelectromechanical) systems, to produce a "lab on a chip", where the polymer's properties of excellent sealing and self-bonding make it an ideal material for microfluidics. Abbasi et al. [2] on the other hand provided an excellent review on the biomedical applications of PDMS while the aerospace applications were discussed in detail by Pielichowski et al. [3]. The elastomeric and flexible nature of silicones has been the subject of attention in wearable electronics and flexible electronics as discussed by Amjadi et al. [4]. Koç and Akça [5] described how to use a PDMS-PVDF composite to design a piezoelectric based tactile sensor that can meet the spatial resolution of the human hand. Other sensing applications of PDMS include thermal sensors fabricated by

1

Parajuli et al. [6] where thermographic phosphors were embedded in a PDMS encapsulant for thin flexible peel and stick sensor design.

As mentioned earlier, Sylgard® 184 (Dow Corning) is one formulation of PDMS that is widely used. It maintains its physical properties over a wide temperature range [7] and has been the material of choice for most of the applications described above. It is also one of the materials chosen for this study. In general, it has a high density of surface charge [8], is classified as hydrophobic [9], and has a low elastic modulus [10]. While most of these are desired properties, high friction [11], and heavy surface fouling [57] cause complications in some applications and will be addressed in this investigation.

Surface and bulk modification of polymers

To overcome some of the challenges of working with and using Sylgard® 184, studies have focused on modifying its bulk and/or surface properties with mixed degrees of success.

Due to its importance to microfluidics, studies focused on modifying Sylgard® 184 wettability are abundant. For example, Bodas et al. [13] showed that exposing Sylgard® 184 to oxygen plasma reduces its hydrophobicity and measured the hydrophobic recovery as a function of time, demonstrating that Sylgard® 184 returns to its natural hydrophobic state in a matter of minutes due to polymer chain migration, while Waddell et al. [9] increased Sylgard® 184 wettability through excimer radiation. This technique however produced cracks on the material surface due to stresses in the formed silica layer. Thermally aging Sylgard® 184 at 100°C for up to 14 days can lengthen the hydrophobic recovery time to the order of days, as demonstrated by Eddington et al. [14], but this technique is very time-consuming, and its benefits are nonetheless temporary. One of the advantages of Sylgard® 184 is its use in rapid

2

prototyping [13], thus, in this study, we endeavored to develop a surface modification technique that is both expeditious and permanent.

Other investigations have discussed efforts related to modifying mechanical properties, particularly tensile and compressive strength. For example, Johnston et al. [11] quantified the effect of curing temperature and time on Sylgard® 184, demonstrating an increase in elastic modulus with both parameters. Carrillo et al. [12] used nanoindentation to characterize elastic modulus at different degrees of crosslinking, showing a softening of Sylgard® 184 as the proportion of crosslinker decreases from the standard 10:1. Campeau et al. [18] quantified the effect of different sterilization techniques on Sylgard® 184 elastic modulus, showing that boiling had a significant effect on the elastic modulus but sterilizing with UV radiation or ethanol did not. These studies showcase how adjusting the fabrication parameters of Sylgard® 184, such as crosslinker ratio, curing temperature, and curing time allow tuning of its elastic properties. Similarly, we aspired to develop a surface modification technique that allows tuning of physical properties of the resulting structure.

Fouling protection is another topic that has been explored in the literature, due to the concern for decreased efficiency of concentrating solar power and photovoltaic installations [58], protein adsorption in biomedical devices [57], clarity degradation of color calibration targets for planetary vehicles [59] and protecting marine equipment from adhering organisms [60], for example. Some of the techniques used for fouling protection include surface functionalization [17], coating with nanoparticles [58], surface texturing [61], and creating new materials with dust-repelling properties [59].

He et al. [15] and Murarash et al. [16] describe different techniques of surface patterning on Sylgard® 184 to tune friction behavior of this polymer, while Vorvolakos and Chaudhury [42] measured PDMS frictional stress as a function of sliding velocity,

demonstrating the existence of a maximum. Landherr [43] investigated the effect that structural modifications and lubrication can have on the friction of PDMS. Pallares et al. [44] investigated the effect of the thickness of a Sylgard® 184 coating on the friction and rupture behavior of a rubber-rubber system. Literature on tuning PDMS friction is relatively less plentiful, presenting an opportunity for contribution. Moreover, there was a possibility of improving the material's performance in biomedicine and aerospace applications and decreasing the need for added lubricants. For this purpose, Silastic™ 3715 was chosen as an anti-fouling, friction-reducing coating for Sylgard® 184 to be investigated.

Frictional force measurement and behavior

Research of frictional behavior must consider the effect of a myriad of parameters that affect the frictional force, such as surface roughness, contact shape, real contact area (RCA), sliding velocity, temperature, material elasticity, adhesion, as well as other mechanical and thermodynamic properties [19, 32, 33, 35]. Nonetheless, theoretical models and numerical simulations have reproduced some experimental observations [22, 24, 26].

The effect of sliding velocity was investigated by Baumberger et al. [19], who demonstrated the bifurcation between stick-slip and sliding regimes. Mohan [23] showed an increase of friction coefficients as a function of the normal force and sliding velocity for aerospace metal alloys, unlike the friction between rubber and a hard surface, which increases with sliding velocity until it peaks, then drops off, as shown by Grosch and others [31, 35-37]. Stick-slip behavior is prominent in Sylgard® 184 friction experimentation and is a topic of concern when investigating shear force behavior.

4

A few of the numerical and theoretical models that have been successfully used to investigate friction are molecular dynamics, Monte Carlo simulation, and the method of dimensionality reduction. Molecular dynamics (MD) simulation has been demonstrated to agree with Amontons' laws in the case of non-adhesive friction [21] and that static friction is determined by the change in potential energy along the sliding direction [22]. Mamalis and Vortselas [24] used Monte Carlo simulation to model single-asperity interactions in the microscale, showing abrasive wear mechanisms. Popov [26-28] introduced the method of dimensionality reduction (MDR), which provides a link between micro- and macro-scale systems of tribological simulation, then discussed the possibility of generalizing MDR to heterogeneous media and applied it to demonstrate how to solve contact problems analytically and numerically. Voll [38] used an MDR-based model to show that adhesive force is inversely proportional to roughness and directly proportional to normal force. However, the effectiveness of these methods in the study of adhesive friction is limited, and elastomer friction is adhesive in nature [33, 40].

There is an inverse relationship between wear rate and the product of strength and elongation at break [32]. Composites with higher heat absorption capacity exhibit higher wear resistance [34]. Chang et al. [39] studied the wear behavior of polyetheretherketone (PEEK) and polybenzimidazole (PBI) at ambient and elevated temperatures and observed the effect of transfer film layers (TFL) on wear rate. One of the purposes of coating PDMS is to reduce or eliminate the effect of friction wear.

Other investigations have shown that the friction-reducing effect of lubricants may become less effective over time [20]. Pogačnik and Kalin [25] clarified how calculated asperity-peak properties are affected by different identification criteria, limiting the predictive power of the technique. Greiner et al. [29] demonstrated that an

inhomogeneous stress field could result in a discontinuity in the microstructure, which may culminate in fracture near the interface. Persson [30] developed a general mean-field theory for the influence of electrostatic attraction between two solids on the contact mechanics, quantifying its tribological effect.

Surface modification techniques that alter the top most layer through mechanical or chemical mechanisms are mostly semi-permanent and have limited durability. In this investigation we have focused on developing a method for passivating the surface of Sylgard® 184 by creating a topcoat layer which is permanently adhered/cured to the base layer. Silastic™ 3715 (Dow Corning) was the material chosen for the top-coat.

Research aims

This work aims to develop, optimize, and fully characterize a process for tuning Sylgard® 184 frictional behavior by creating a top coat layer from Silastic™ 3715 (Dow Corning) [45]. Silastic™ 3715 in bulk form has low frictional behavior and is well-recognized for its antifouling properties [45]. A significant part of this investigation is to fully characterize surface and bulk properties of the bilayer and testing the efficacy and reproducibility of two coating methods employed in this study. The effect of temperature and coating thickness will also be quantified. The two different deposition methods chosen are: spin coating and drop casting. In brief, the goals of this study are: (1) Develop a protocol to fabricate a bilayer structure composed of Sylgard® 184 substrate and Silastic™ 3715 topcoat, (2) Characterize surface and bulk properties of Sylgard® 184, (3) Characterize surface and bulk properties of bilayer structure, and (4) Optimize fabrication protocol for bilayer integrity and low friction.

Thesis outline

Chapter 2 provides an overview of the theories relevant to the research. Chapter 3 describes the materials and methods used to fabricate and prepare samples and experimental techniques that characterized their properties. Chapter 4 presents and discusses results and measurements. Finally, chapter 5 proposes conclusions derived from the results and possible avenues of further investigation and improvement of methods.

2. Theory

In this chapter, an overview of relevant theories is presented. For the sake of brevity, the scope has been limited to only those topics most directly linked to the study.

Frictional force

Friction, like adhesion, is a reaction force, internal to the system. Amonton and Coulomb defined the frictional force as

$$F = \mu L \qquad\qquad (1)$$

where the tangential force F is proportional to the normal load L and a constant coefficient $\mu = F/L$, independent of the apparent area of contact or the sliding velocity. However, equation (1) is not valid if there is adhesion in the interface. In that case, the frictional force can be redefined as

$$F = \mu (L_o + L) = F_o + \mu L \qquad\qquad (2)$$

where the more general $\mu = dF/dL$ is accepted, and F_o accounts for adhesive forces. F_o is proportional to the real contact area, $F_o = \tau RCA \propto L^\alpha$, where α depends on the elasticity or plasticity of the material asperities. The RCA may be well below the apparent area A (if the surface is hard), or well above A (if the surface is soft). This allows us to split the frictional force into load-dependent and adhesion-dependent contributions [21]. Adhesion is the basic mechanism of friction for polymers in a highly elastic state; mechanical losses due to deformation contribute more when it is in a glassy state [35]. However, determining the RCA is very challenging; there are no experimentally verified criteria about how to define "actual" load-carrying asperities, and arbitrarily selected asperity identifying criteria (3/5/7-point peak, peak-threshold value, data resolution) affect calculated asperity properties such as number, radii, and heights [25].

The coefficient of friction depends on many factors, such as material, sliding velocity, surface roughness, humidity, geometry, temperature, molecular weight,

mechanical vibrations, and electric fields [21, 30, 36, 41, 42]. The stick-slip motion observed in rubber sliding arises when the force-velocity curve has a negative slope, in which case a coefficient of friction cannot be determined as F_s and F_k depend on the inertia of the system [21]. In rubbers, τ (and therefore frictional force) depends on temperature; at $T > T_g$, τ dependency on T is determined by molecule segment mobility at the interface, while at $T < T_g$, τ is nearly velocity independent and has similar magnitude as glassy polymers [41]. PDMS friction decreases with molecular weight [42] and with a reducing RCA, because adhesion force has less effect on contacts with higher loads [15].

When two surfaces approach each other, their opposing asperities with maximum height come into contact. As the load increases, new pairs of asperities with lesser height make contact forming individual spots. The overall area of these spots is known as the real contact area. The relationship between the load and asperity deformation, resulting in different RCA, depends on the elastic modulus of the material. Asperities can experience elastic, plastic, or viscoelastic deformation, followed by dissipation of mechanical energy. When a polymer with viscoelastic behavior slides against a hard, rough surface, the energy dissipation occurs due to high hysteresis losses, a deformation component known as friction due to elastic hysteresis. Energy may be also carried away with elastic waves generated at the interface and outgoing to infinity, owing to nucleation and development of microcracks in the material. The asperities of the harder surface are assumed to plough the softer one, this ploughing is accompanied by adhesion. Polymers are very sensitive to frictional heating, resulting from deformation at contact points and from breaking adhesive bonds. The temperature change affects hardness and shear strength, which affects the frictional force [35].

9

Amonton's first law has been experimentally found to hold for some polymers under certain conditions within a limited range of loads; below that the coefficient of friction decreases with increasing load due to elastic deformation of the surface asperities, above that the coefficient increases with increasing load due to plastic deformation of asperities in contact. Speed-independent friction was found only within a limited range of velocities for some polymers; for low velocities the viscous resistance in the contact zone increases with increasing velocity; for high velocities elastic behavior is prevalent in the contact zone and the frictional force depends only slightly on the velocity or it decreases with velocity; in the intermediate range of velocities the above factors are in competition and a maximum appears in the frictional force-sliding velocity curve [35].

In this study, we will limit the scope of the investigation to the effects of a coating and of temperature, bypassing the need to distinguish between load- and adhesion-dependent contributions, looking instead at the relative values of the total frictional force.

Force of adhesion

When two surfaces are brought into contact, the forces of repulsion and attraction between the atoms and molecules balance each other at a certain distance $z = z_0$. In polymers: Van Der Waals and hydrogen bonds are common [35]. The adhesive force is inversely proportional to the roughness and the shear modulus and proportional to the normal force [38]. Static friction indicates the interface is trapped in a potential well, while kinetic friction is associated with energy dissipation. The origin of static friction is in weakly adsorbed mobile molecules, glassy interface films, material transfer, elastic deformation, and surface roughness [22].

Adhesion is characterized by the work of separating bonded interfaces. This work fluctuates during sliding, hills and valleys on surface correspond to maxima and minima of the interfacial energy density. Static friction, F_s, is the force needed to overcome that energy barrier, and corresponds to the maximum variation of interfacial energy density over sliding distance [22].

Wear behavior

Material transfer occurs when interfacial bonding is stronger than cohesive bonding. Generally, in polymers, interfacial and cohesive forces are nearly equal, so fracture often occurs in the bulk. Changes in surface layer arise from mechanical stresses, temperature, and chemical reactions, and the local temperature at the interface may be substantially higher than that of the environment [35].

Adhesion wear results from the shear of the friction junctions. Transfer of material from one surface to another occurs due to localized bonding between the contacting solid surfaces. A thin film of soft material is transferred onto the hard mating surface. If the transferred polymer film is carried away from the hard surface and is newly formed, the wear rate is increasing. In the case that the film is held in place, the friction occurs between similar materials that may result in seizure. One consequence of polymer transfer is a change in roughness of both surfaces in contact. The roughness of the polymer surface undergoes large variation during the unsteady wear until the steady wear is reached, while counterface surface roughness is modified due to transfer of polymer. Polymers are most susceptible to adhesion wear transfer when sliding against metals and polymers [35].

Friction contacts undergo cyclic stressing at rolling and reciprocal sliding. In addition, each asperity of friction surface experiences sequential loading from the

asperities of counterface. This results in material fatigue in these regions that leads to the generation and propagation of cracks and the formation of wear particles. Loss of material from solid surfaces owing to friction fatigue is referred to as fatigue wear [35].

Abrasive wear relates to cutting or plowing of the surface by harder particles or asperities, whose rates depend strongly on the shape and apex angles of the abrasive points [35]. In abrasive wear there is a nearly linear relationship between wear rate and $1/\sigma_u\epsilon_u$, where σ_u is the ultimate tensile stress and ϵ_u is the corresponding strain, but in steady-state sliding conditions this relationship no longer applies because of the complicating effects of mass transfer from the polymer to the counterface. The volume of wear is always directly proportional to the distance of sliding [32].

Elasticity of materials

Stress,

$$\frac{\delta F}{\delta A} \qquad (3)$$

where F is the external force and A the area where it is applied, can be decomposed into 3 normal components (σ_x, σ_y, σ_z) and 3 distinct tangential, or shearing, components (τ_{xy}, τ_{yz}, τ_{zx}). Similarly, strain, the change in dimensions of an object initially of lengths u, v,

w, can be decomposed into 3 normal components and 3 tangential, or shearing, components:

$$\epsilon_x = \frac{\partial u}{\partial x}, \epsilon_y = \frac{\partial v}{\partial y}, \epsilon_z = \frac{\partial w}{\partial z} \qquad (4)$$

$$\gamma_{xy} = \frac{\partial u}{\partial y} + \frac{\partial v}{\partial x}, \gamma_{yz} = \frac{\partial v}{\partial z} + \frac{\partial w}{\partial y}, \gamma_{zx} = \frac{\partial w}{\partial x} + \frac{\partial u}{\partial z} \qquad (5)$$

From Hooke's Law, elongating stress in the z direction will result in strain

$$\epsilon_z = \frac{\sigma_z}{E} \qquad (6)$$

where E is the modulus of elasticity in tension, or Young's modulus. This will be accompanied by lateral contractions

$$\epsilon_x = -\nu \frac{\sigma_z}{E}, \epsilon_y = -\nu \frac{\sigma_z}{E} \qquad (7)$$

where ν is a material-dependent constant called Poisson's ratio [46].

For elements where w >> u, v, A = uv may be assumed constant during elongation, such that

$$\sigma_z = \frac{F}{A}, \epsilon_z = \frac{L - L_o}{L_o} \qquad (8)$$

where L_o is the initial w and L is w after elongation [47]. Therefore,

$$E = \frac{F}{A} \frac{L_o}{L - L_o} \qquad (9)$$

Similarly, G, the elastic modulus of elasticity in shearing is defined as [46]

$$G = \frac{\tau_{xy}}{\gamma_{xy}} = \frac{\tau_{yz}}{\gamma_{yz}} = \frac{\tau_{zx}}{\gamma_{zx}} = \frac{E}{2(1 + \nu)} \qquad (10)$$

The moduli of elasticity are temperature dependent

$$E = E_o \exp\{-\beta T\} \qquad (11)$$

where β is the rheological parameter [35].

Optical density

Optical density is sometimes defined as the absolute value of the logarithm of base 10 of the power transmission factor of an optical attenuator [48]:

$$OD = -\log \frac{P_{out}}{P_{in}} \qquad (12)$$

Other sources [49] call the quantity above absorbance and define optical density as the absorbance normalized by the optical length:

$$NOD = \frac{A}{L} = -\frac{1}{L} \log \frac{P_{out}}{P_{in}} \qquad (13)$$

This study will use the definition in equation (12).

Interfacial electric potential

Applied electric voltage between two solids often result in the accumulation of charges of opposite signs on the interfaces. This results in an electrostatic attraction, denoted electroadhesion, which adds to the external load and increases the area of contact and the sliding frictional force [30]. In metal-polymer interfaces, the metal is usually the electron donor [35].

Interfacial free energy

The adhesion between any materials is a function of their surface free energy components, where the adhesion force is developed at the molecular level. The atoms at surface have lower level of bond energy compared to the atoms in bulk. As molecules in the material bulk are surrounded by other molecules from all sides, an external work must be applied to create a new surface area. This work is known as the total surface free energy of the material(γ). The Sessile drop method is commonly used to measure the surface free energy between a probe liquid and solid surface by means of measuring the contact angle (θ) between a droplet of a selected probe liquid (L) and solid (S)

14

surface immersed in a vapor (V). The Young's equation defines the equilibrium between the three phases [40, 50]

$$\gamma_{SV} = \gamma_{SL} + \gamma_{LV} \cos \theta \qquad (14)$$

Fracture mechanics

Fatigue is a change in the material state due to repeated (cyclic) stressing which results in progressive fracture. Its characteristic feature is accumulation of irreversible changes, which give rise to generation and development of cracks [35]. Once formed, cracks propagate following either the Paris law, in low stress (under half of the material's yield stress)

$$\frac{dl}{dN} = C_1 \Delta K^m \qquad (15)$$

where l is the crack length, N the number of cycles, ΔK the stress range in a cycle, and C_1 and m are material constants; or, in the case of high stress, following

$$\frac{dl}{dN} = C_2 \sigma^n l \qquad (16)$$

where σ is the average stress in a cycle, and C_2 and n are material constants [51].

Phosphor thermometry

A phosphor is thermographic when one or more of its luminescence properties is temperature dependent. One such property is luminescence intensity, which decays following the equation

$$I = I_o \exp\{-\beta t\} \qquad (17)$$

where I is intensity at the time t, I_o is initial intensity, and β is the rate of decay, a temperature-dependent material constant. By recording emission intensity over time, β can be calculated as the negative of the slope of $\ln(I/I_o)$ over t, then compared to material results from known temperatures [52, 53].

15

3. Materials and methods

This chapter describes in detail all the steps taken to create the bilayer structure mentioned previously and all the characterization methods that were employed. A variety of bulk and surface characterization techniques were used to fully understand the behavior of the bilayer structure and it was briefly tested for a possible application to demonstrate proof of concept. Layer 1 (L1) consisted of the elastomer Sylgard® 184 and Layer 2 (L2) consisted of Silastic™ 3715 topcoat. The topcoat was created either by spin coating or by drop casting methods.

Bilayer synthesis and preparation

Substrate preparation (L1)

To fabricate the bilayer, first a Sylgard® 184 thin substrate was produced to form L1. This step was followed by creating L2 which involved a Silastic™ 3715 topcoat which was deposited either by spin coating or drop casting methods. For each chosen spin coating speed and for drop casting method, four samples (n=4) were created, except for 6.00K rpm, (n=2), and 8.00K rpm (n=1), where technical issues related to the spin coating system limited the fabrication number. Four separate samples were also prepared and kept without a topcoat to serve as the controls (L1 only). In some cases, thermographic phosphors were introduced also and will be discussed later in the document. Figure 2 shows schematic diagrams of the prepared samples and a summary of the sample types is presented in Table 1.
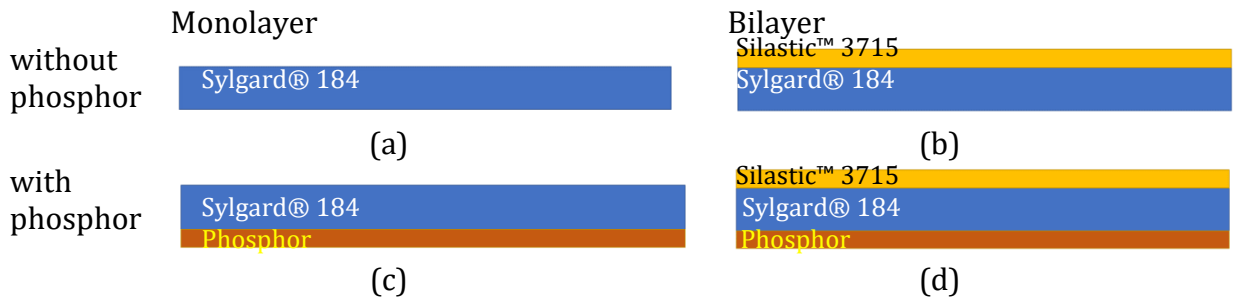
Figure 2: Schematic diagram of bilayer and monolayer samples.

Table 1: Summary of sample types and number.

Sample type	Number
Drop cast	4
Spin coated 0.64K rpm	4
Spin coated 1.03K rpm	4
Spin coated 2.04K rpm	4
Spin coated 4.09K rpm	4
Spin coated 6.00K rpm	2
Spin coated 8.00K rpm	1
Uncoated	4

To prepare the substrate layer (L1) first a series of Sylgard® 184 samples were prepared with increasing amounts of crosslinker to base polymer ratio and fully characterized. This was done in order to determine the optimum ratio of crosslinker to base polymer for our purpose. Once determined, for all samples these same conditions were used. All materials and chemicals were measured on an Ohaus© Pioneer™ microbalance. To prepare L1, prepolymer:crosslinker (10:0.5) was combined into a slurry and vigorously mixed for 2 min, until a uniform viscosity was achieved. The slurry was poured into cylindrical aluminum molds 44 mm in diameter (nominal), accommodating 1 g of material. The substrates were completely outgassed in an Across International AccuTemp vacuum oven at room temperature for approximately 20 min, until all air bubbles were eliminated. They were then cured for 45 min at 100°C. After curing was complete, the substrates were removed from the oven and allowed to cool to

17

room temperature, then gently peeled from the molds, resulting in uniform disks of 44 mm diameter and 1 mm height, as desired.

Topcoat preparation (L2)

To prepare the topcoat layer (L2) Silastic™ 3715 prepolymer base and crosslinker were measured using an Ohaus® Pioneer™ microbalance, combined at a 7:3 ratio and vigorously mixed for 2 min, until a homogeneity was achieved. The mixture was outgassed at room temperature in an Across International AccuTemp vacuum oven for 15 min, which resulted in 90% elimination of air bubbles. Complete outgassing would have required at least 30 min due to the mixture's high viscosity, at which point the prepolymer base and crosslinker would have begun to separate. This in turn would have prevented the mixture from curing correctly. So, it was decided to abort the outgassing step once 90% outgassing efficiency was reached.

Topcoat deposition (L2)

To create the second layer two methods were employed.

Spin coating: Four of the samples prepared in section 3.1.2 were spin coated at increasing speeds (ω=0.64K rpm, 1.03K rpm, 2.04K rpm, and 4.09K rpm). Another set of two was spin coated at ω=6.00K rpm, and ω=8.00K rpm, producing a range of topcoat thicknesses (d) that were later measured and characterized. Control substrates were kept separately for further investigation and comparison. The spin coating step was performed using a Chemat Technology KW-4A spin coater, secured using a Gast Manufacturing DOA-V722-AA vacuum pump, and the topcoat mixture was poured onto the substrate. The spin coater was activated; first at 0.64K RPM for 9 s, then at the final speed ranging from 0.64K rpm to 8.00K rpm for 30 s. Technical issues related to spinning at ω > 5.00K rpm limited the number of samples that were successfully prepared for 6.00K and 8.00K rpms.

Drop casting: To create L2 by means of drop casting, cleaned samples were placed on a Stovall Life Science Belly Button tilt table and a known volume of the topcoat mixture was poured onto the substrate. Then the tilt table was activated for 2 min, allowing the topcoat mixture to distribute an even layer on the substrate and the excess to overflow.

After deposition, all samples (bilayers and monolayers) were placed in an Across International AccuTemp vacuum oven at room temperature, and the oven was brought up to 100°C. As the oven heated to the desired temperature the samples were gradually curing and only required a further 5min heating at 100°C to complete the curing stage. This gradual heating resulted in better topcoat integrity than samples that were cured in an oven that was preheated at 100°C. The entire protocol is summarized in Figure 3.

Substrate

```
Mix parts in 10:0.5 ratio
        ↓
    Pour into mold
        ↓
   Outgas for 20 min
        ↓
  Heat oven to 100°C
        ↓
   Place in hot oven
        ↓
  Cure in oven for 45 min
        ↓
   ( Peel from mold )
```

Topcoat

```
   Mix parts in 7:3 ratio
        ↓
    Outgas for 15 min
       ↙        ↘
Pour onto base      Pour onto base
secured by         on tilt-table
vacuum to          and activate it
spin-coater        for 5 min
and activate it
       ↘        ↙
    Place in RT oven
        ↓
  Heat oven to 100 °C
        ↓
  ( Cure in oven for 5 min )
```
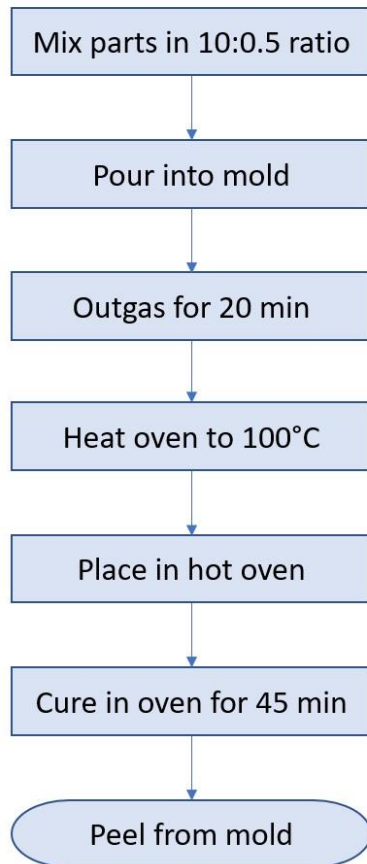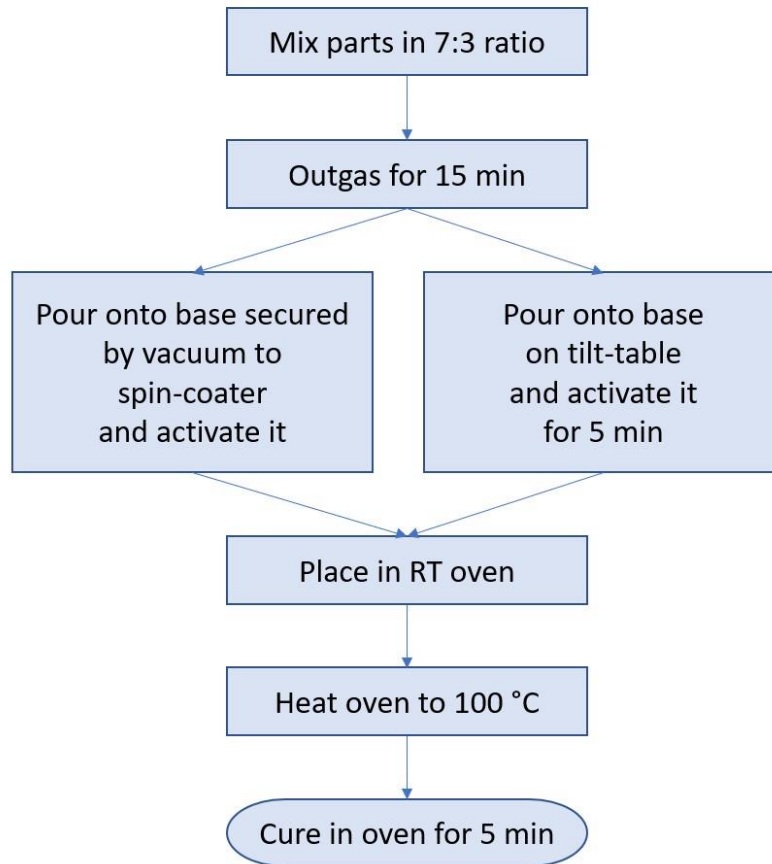
Figure 3: Flowchart of bilayer preparation protocol.

Bilayer characterization

Optical characterization

All microscopy images were taken using a Unitron Examet-4 microscope with a Unitron 319CU 3.2MP CMOS camera and Micrometrics SE Premium software. For surface images, sample surfaces were cleaned with isopropyl alcohol prior to imaging. Samples were placed on glass slides to minimize handling and imaged at three distinct locations (1) the center, (2) near the edge, and (3) halfway between 1 and 2. For cross-sectional images, samples were cut into thin (< 1 mm) strips and cleaned with isopropyl alcohol. Strips were placed sideways on glass slides and imaged at 3 different positions.

Microscope software was used to measure topcoat thickness (d) and other forms of image analysis.

Surface profilometry

To understand the effect of spin coating rotational speed on surface roughness, surface profilometry was performed. Samples were placed on a Filmetrics Profilm3D Optical profilometer stage and imaged using Profilm software at 10x magnification.

Frictional force measurement

Room temperature measurements: To perform frictional force measurements, specimens were cut into 5 mm x 5 mm squares and placed on a Mark-10 COF Fixture 200 g steel sled for adherence. Sled and sample were weighed together on an Ohaus CS 2000 microbalance and the result was entered in the Mark-10 M5-2-COF force gauge. The sled was attached to the force gauge by an inelastic string passing through a pulley, which was connected to the COF fixture steel platform. The force gauge traveled up a Mark-10 ESM303 test stand at 300 mm/min, pulling the sled and sample along the platform, while the MesurGauge software recorded frictional force, travel, and time (schematic diagram of the setup shown in Figure 4). Each sample type was tested at least 3 separate times. The static friction force was calculated by finding the first peak of the recorded data, and kinetic friction force was calculated by averaging the 100 data points after the first peak. This process was automated using Python (full code presented in Appendix A).
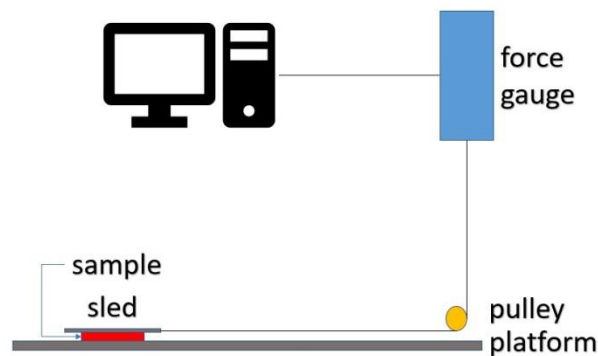
Figure 4: Friction test diagram.

Low Temperature Measurements: For low temperature measurements, specimens were cut into 5 mm x 5 mm squares and placed inside a LN_2 dewar (T=77 K) and stored overnight. Before testing, LN_2 was poured onto the Mark-10 COF Fixture to cool the entire system down prior to taking measurements. Next, each sample was removed from the dewar and tested as previously described. Each sample type was tested 3 separate times. The MesurGauge software was used to record coefficient of friction, travel, and time starting when samples were exposed to room temperature air. The time data was used to estimate sample temperature during testing, by comparing it to previous experiments of temperature change over time.

Elastic modulus evaluation

Tensile testing: To perform tensile tests, an ASTM D-1708 die was used to cut dog bones from bilayer and monolayer samples. Due to the brittle nature of Silastic™ 3715, the drop cast topcoat samples fragmented, so it was not possible to perform tensile tests on those. The dog bones were clamped with serrated-faced grips attached to the base of a Mark-10 ESM303 test stand and one of the force gauges available (listed in Table 2). The test stand was activated at a rate of 15.0 mm/min and load, travel, and time recorded by the MesurGauge software. Each sample type was tested at least 3 separate times. A diagram of the test setup can be seen in Figure 5. The stress and the strain were

calculated for all samples. The relaxed cross-sectional area, measured by a Mahr 40 EX micrometer and the relaxed length, nominally 15 mm, were used for calculations.

Table 2: Force gauges used for tensile tests.

Brand	Model	Max. load	Precision
Mark-10	M5-5	25 N	0.025 N
Mark-10	M5-20	100 N	0.1 N
Mark-10	M5-100	500 N	0.5 N
Mark-10	M5-2-COF	10 N	0.01 N
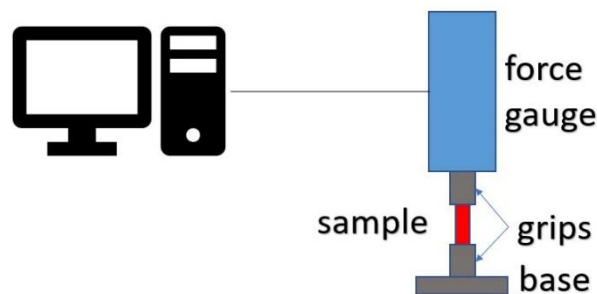
Figure 5: Tensile elastic modulus test diagram.

Compression testing: For the compression tests, disk-shaped samples were placed on the base of a Mark-10 ESM303 test stand with a flat 12.8 mm diameter pin (measured with a Mahr 40 EX micrometer) attached to one of the force gauges in Table 2. The test stand was activated at a rate of 15.0 mm/min while the MesurGauge software recorded time, travel, and load. Each sample type was tested 3 separate times. The stress was calculated by dividing load by the area of the pin. The strain was calculated by dividing travel by the relaxed thickness of the sample, measured by a Mahr 40 EX micrometer. Results were plotted for comparison, but the linear portion was too short to allow for compressive elastic modulus calculation.

Peel strength measurement

In order to evaluate the bond strength of Silastic™ 3715 to Sylgard® 184 180° peel tests were performed using a Mark 10 system. First, to serve as a control, the peel strength of Sylgard® 184 to itself was tested. Next, the peel strength of Silastic™ 3715 to Sylgard® 184 was tested.

Sylgard® 184-Sylgard® 184 bond strength: In the first case, samples were prepared by sandwiching Sylgard® 184 mixed at increasing crosslinker ratios between strips of aluminum foil, then outgassing and curing as described in subsection 3.1.1. Then each strip was clamped with a serrated-faced grip attached to the base of a Mark-10 ESM303 test stand and one of the force gauges in Table 2. The test stand was activated at a rate of 300.0 mm/min while the MesurGauge software recorded time, travel, and load.

Sylgard® 184-Silastic™ 3715 bond strength: In the second case, samples were prepared by pouring Sylgard® 184 mixed at 10:1 crosslinker ratio on strips of aluminum foil, then outgassing and curing as described in subsection 3.1.1, then pouring Silastic™ 3715 mixed at 7:3 crosslinker ratio and outgassing and curing as described in subsection 3.1.3. Then the strip was clamped with a serrated-faced grip attached to the base of a Mark-10 ESM303 test stand and the edge of the Silastic™ 3715 layer was clamped with another such grip attached to one of the force gauges in Table 2. The test stand was activated at a rate of 300.0 mm/min while the MesurGauge software recorded time, travel, and load.

In both cases, to calculate peel strength, the load was divided by the width of the strips. Maximum and average peel strengths were graphed and analyzed.

UV-Vis spectroscopy

In many applications Sylgard® 184 is used as an encapsulant and the material is used for its optical clarity and transparency. To better understand how the addition of the topcoat affects transparency, spectroscopy was performed. Disk-shaped samples were loaded in a Thermo Scientific UV-Vis spectrometer model Evolution 220. Reflectance (R) and transmittance (T) data were collected as a percentage of emission

for a range of wavelengths by the Thermo Insight software. Scatter (S) was calculated by subtracting R and T from 100%.

Surface charge evaluation

To understand how the addition of the topcoat affects the surface charge and quantify the contribution of electroadhesion to the work of friction, surface potential was measured. Disk-shaped samples (bilayer and monolayer) were placed on a custom-made stand holding an oscillating Kelvin probe head. A Trek Model 325 Electrostatic voltmeter measured the electric potential difference between the sample surface and ground.

Contact angle

To understand how the topcoat affects the hydrophobicity and wettability of the interfacial system, quantifying the contribution of surface free energy to molecular bonding and adhesion, contact angle was measured. Samples were placed on the platform of an AST Products Inc. VCA Optima goniometer and 5 μL of deionized water were dropped by a precision syringe. VCA Optima XE software measured the triple interface angles.

Fatigue cycling

To understand how well the topcoat tolerates fatigue wear and retains its integrity, a fatigue cycling experiment was performed. Rectangular samples were cut and clamped with serrated-faced grips to the base of a Mark-10 ESM303 test stand and to one of the force gauges in Table 2. The stand was activated at a rate of 15.0 mm/min to elongate the sample to 20% strain, then return to resting position n_c times, where n_c varied from 1 to 850. The MesurGauge software recorded time, travel, and load. Afterwards, the samples were imaged in a Unitron Examet-4 microscope with a Unitron 319CU 3.2MP CMOS camera and Micrometrics SE Premium software.

Phosphor thermometry

To evaluate the feasibility of and usefulness of the Silastic™ topcoat for applications of the bilayer system, phosphor thermometry measurements were performed. The motivation behind this testing was to investigate if it was possible to (1) excite the embedded phosphor layer in the Sylgard® 184 layer (L1) coated with the protective topcoat layer (L2) using the same optics as would have been used otherwise. To accomplish this, samples were prepared with a bottom layer of 10% $Mg_3F_2GeO_4$:Mn-doped Sylgard® 184, a middle layer of pure Sylgard® 184, then spin coated with Silastic™ 3715 at three different speeds (1.01K rpm, 2.01K rpm, 4.01K rpm). One uncoated sample was also made as a control. Each sample was then placed on a MK 100 Instec heating and cooling stage at different temperatures (100°C, 25°C, -50°C) and excited with a 405 nm LED (Thorlabs). The emitted signal was measured by a Tektronix 2012 C digital oscilloscope and analysis protocol described in detail by Aryal and Parajuli was used [52, 53].

4. Results and discussion

This chapter presents the results of the characterization techniques described in chapter 3. Some of the challenges are discussed and interesting results are highlighted. Conclusions drawn from these results are presented in chapter 5.

Microscopy

To determine the degree of homogeneity of the substrates before and after coatings, multiple images were taken with a metallurgical microscope from 3 different areas of each sample, with magnifications ranging from 5x to 50x. After careful inspection of the surfaces it was concluded that both coating techniques lead to 100% coverage of the samples.

(a) (b)
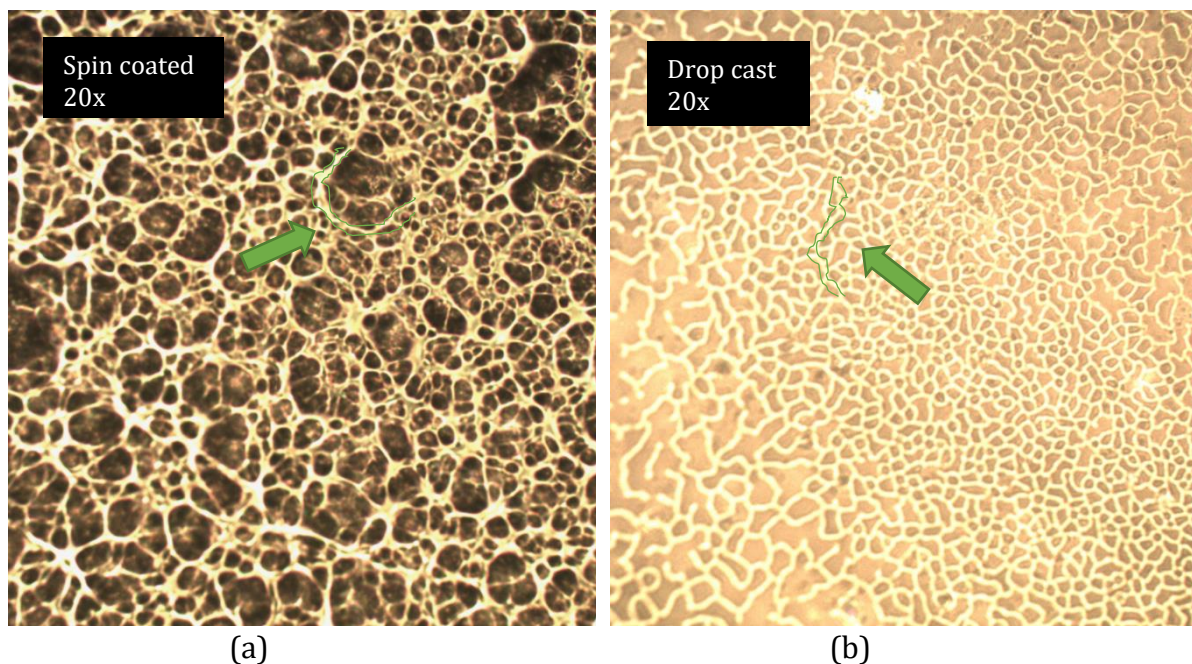
Figure 6: 20x magnification of (a) 6K rpm spin coated Silastic™ 3715 on Sylgard® 184, (b) drop cast Silastic™ 3715 on Sylgard® 184, showing the homogeneity of surfaces under both deposition methods.

Figure 6 (a) and (b) show the surface of a sample after (at 20x magnification) the two different deposition techniques have been completed. In (a) a sample is shown where Silastic™ 3715 was spin coated at 6.00K rpm, resulting in a uniformly distributed

pattern of polymer filaments (the lighter color, highlighted in green) coating the surface. In (b) a drop cast sample is shown, where the pattern displays the slight separation of prepolymer and crosslinker due to the delay between mixing and curing, for outgassing. We attempted to achieve a balance between removing as much of the gas in the mixture and reducing the outgassing time to minimize that separation and were able to reach 90% gas removal in 15 min.

To measure the thickness of the coating (d) as a function of spin coating speed (ω), coated samples were sectioned into thin slices and imaged cross-sectionally. Microscope imaging software (Micrometrics SE Premium) was used to measure the desired parameters at multiple locations and then averaged. A microscope calibration slide was used to get accurate length measurements. Figure 7 shows cross-sectional images of spin coated samples, with the material interfaces highlighted in green, where we can distinguish between Sylgard® 184 (transparent) and Silastic™ 3715 (semi-transparent). We observed that the coating thickness (d) for Silastic™ 3715 has a nonlinear dependence on spin coating speed (ω) and can be tuned to the desired magnitude by adjusting the spin coating speed. The results are presented in Table 3 and the corresponding graph is presented in Figure 8.
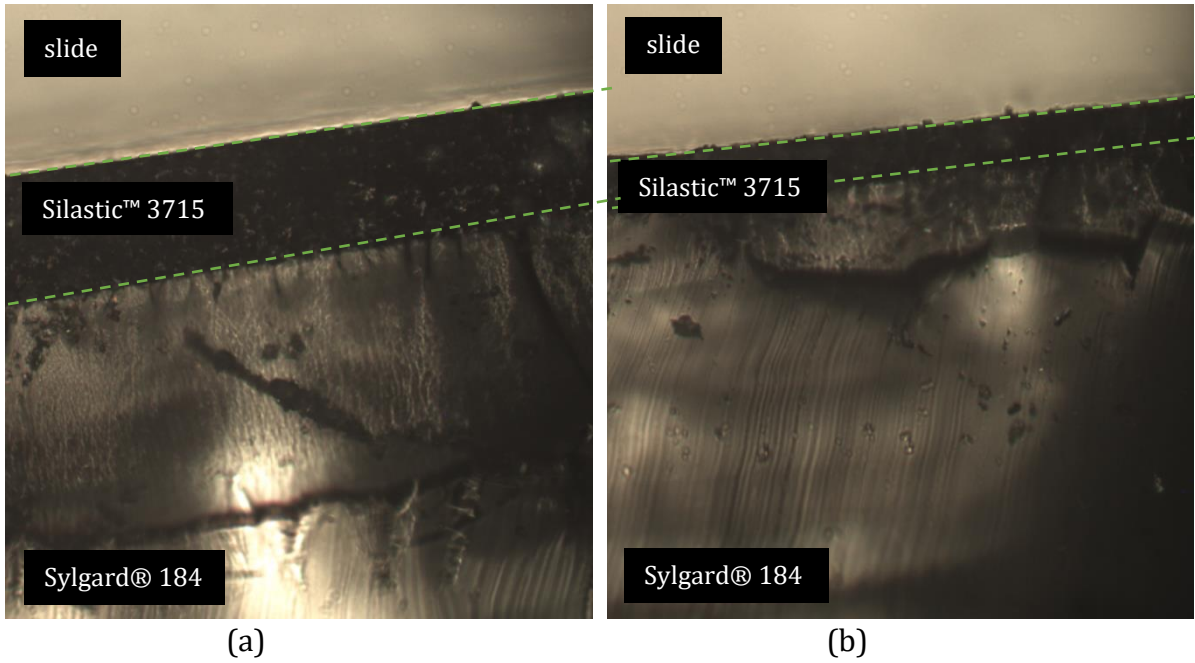
Figure 7: 10x cross-section images of spin coated samples, with highlighted interfaces between substrate and topcoat, and topcoat and slide. (a) 0.64K rpm, (b) 1.02K rpm, showing the difference in topcoat thickness due to spin coating speed.

Figure 8: Topcoat thickness (d) as a function of spin coating speed (ω), showing an inverse nonlinear relationship between them. n=3

The relationship between topcoat thickness (d) and spin coating speed (ω) seen in

Figure 8 is consistent with the behavior expected from viscous fluids and fits the

following equation [54]:

$$d = \frac{C}{\omega^{\alpha}} \qquad\qquad (18)$$

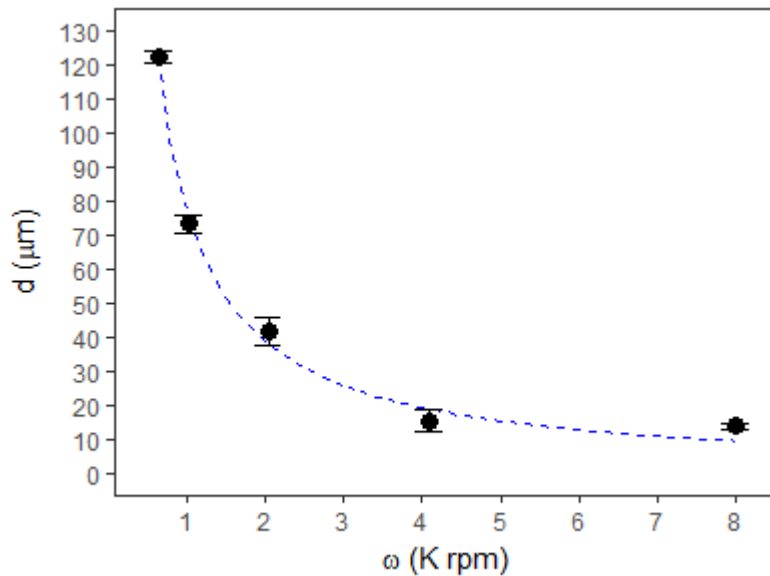where d is the topcoat thickness, ω is the spin coating angular speed, C is a proportionality constant, and α is an exponent unique for each material (α=1.14 for Sylgard® 184) [54]. Here, we used the least squares method to calculate values for Silastic™ 3715: C = 0.078 ± 0.002, and α = 0.98 ± 0.06 with 95% confidence (R^2 = 0.994).

Table 3: Spin coating angular speed (ω) and topcoat thickness (d). n=3

ω (K rpm)	d (μm)
0.64	122.5±1.7
1.03	73.3±2.5
2.04	41.9±3.9
4.09	15.5±3.3
8.00	14.0±0.8

Surface profilometry and roughness

To better understand the surface profile of the new material and to determine the role that surface roughness might play on friction, profilometry measurements were conducted on each sample type. Non-contact profilometry was performed by means of white light interferometry (WLI) and phase-shifting interferometry (PSI) with a resolution of 0.05 μm. In each case multiple locations were imaged and fully characterized.
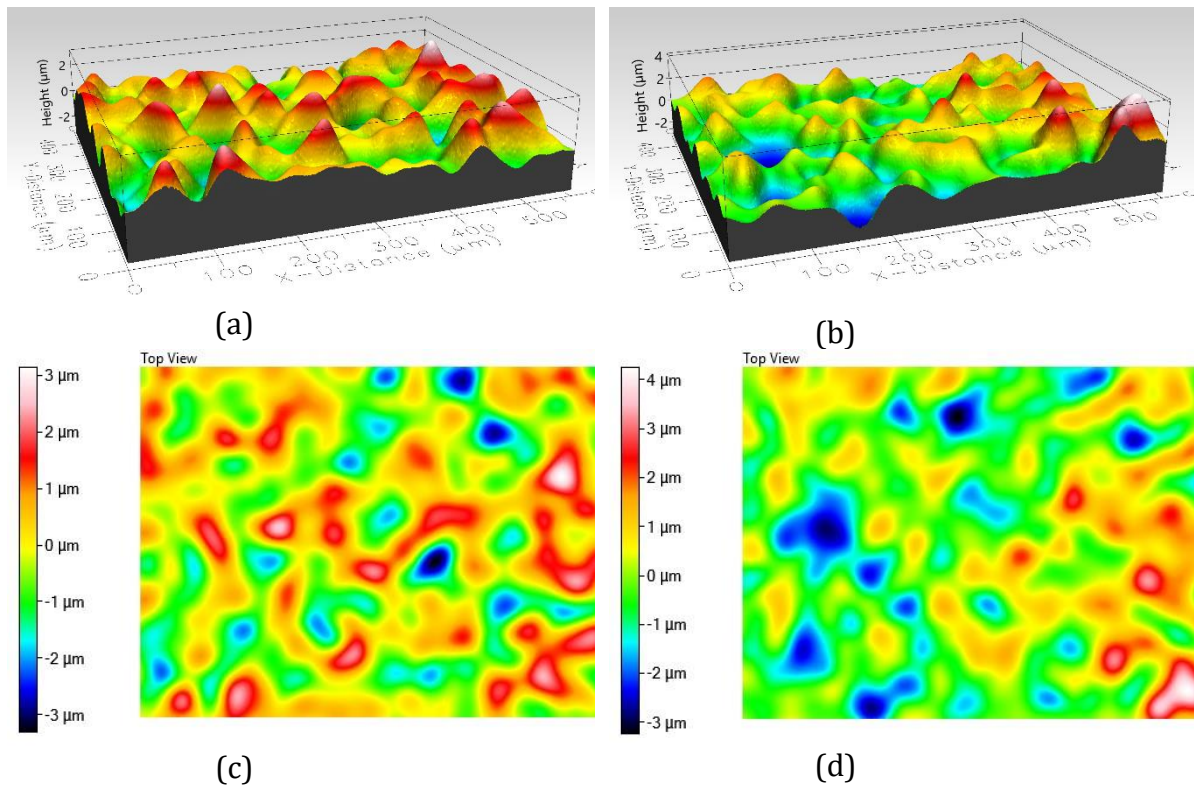
Figure 9: Profilometry of (a) 3D view of 0.64K rpm spin coated sample, (b) 3D view of 4.06K rpm spin coated sample, (c) top view of 0.64K rpm spin coated sample, (d) top view of 4.06K rpm spin coated sample, showing the similarity in peak-to-valley distances and difference in peak-to-peak distances.

Figure 9 (a) and (b) show representative 3D views of samples spin coated at 0.64K rpm and 4.06K rpm respectively. We can see that in both cases the peak-to-valley heights (h) are approximately 6µm. The results for all samples are summarized and presented in Table 4, and separately graphed in Figure 10. Figure 9 (c) and (d) show top views of the same 0.64K rpm and 4.06K rpm spin coated samples, where we can observe the differences in peak-to-peak distance, which increases with spin coating speed. We expected to see a significant difference in the peak-to-valley heights between uncoated Sylgard® 184 and Silastic™ 3715 coatings, as this could explain the observed difference in frictional forces of the samples (presented later this chapter), and because of the tactile differences between those surfaces. Given that all the peak-to-valley heights are approximately the same for all samples, we conclude that surface roughness does not appear to dominate the variation in frictional forces observed for these samples.

31

Table 4: Peak-to-valley distance (h) as a function of topcoat thickness (d). n=3

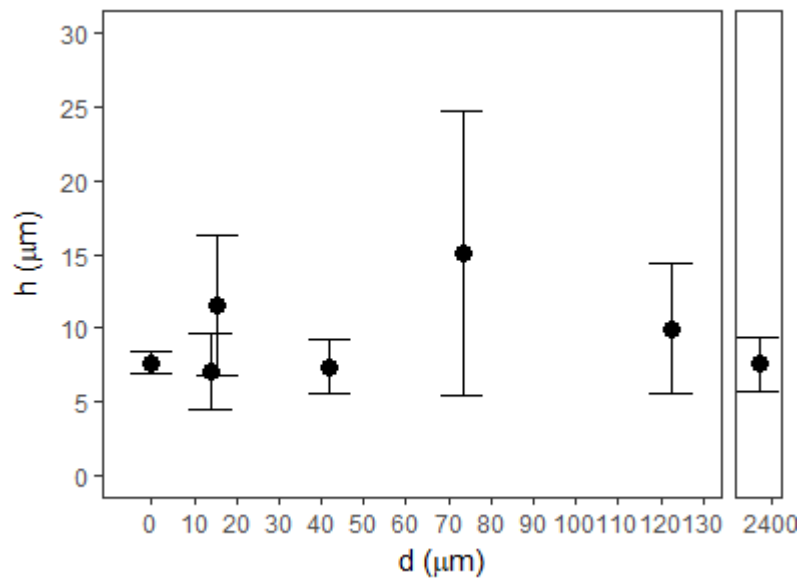| d (µm)	h (µm)
0 (uncoated Sylgard® 184)	7.7 ± 0.7
14.0	7.1 ± 2.5
15.5	11.6 ± 4.7
41.9	7.4 ± 1.8
73.3	15.1 ± 9.6
122.5	9.9 ± 4.4
2397 (drop cast Silastic™ 3715)	7.6 ± 1.9

Figure 10: Peak-to-valley distance (h) as a function of topcoat thickness (d), showing no apparent correlation between them. n=3

Contact angle investigation

An important factor influencing materials interfacial behavior (e.g. adhesion, friction) is the surface energy of the material reflected in its level of hydrophobicity / hydrophilicity. Thus, the contact angles for Sylgard® 184 and Silastic™ 3715 were measured at room temperature. These values are presented in Figure 11 and summarized in Table 5. It was observed that drop cast Sylgard® 184 and drop cast Silastic™ 3715 had similar levels of hydrophobicity, both $\theta > 90°$ and are classified as hydrophobic as opposed to super hydrophobic which would require contact angles $\theta > 150°$ [56]. Samples that were spin coated all displayed contact angles ranging from 84°

to 110° also displaying hydrophobic behavior. As there does not appear to be a trend for θ and d, the variation in frictional force appears not to be due to a difference in surface free energy. However, we can't rule out that the resolution of the measuring device may not be high enough to show the trend, if it exists.

Table 5: Contact angle as a function of topcoat thickness (d). n=6

d (μm)	Contact angle (°)
0 (uncoated Sylgard® 184)	93.2 ± 1.5
14.0	102.0 ± 5.0
15.5	107.6 ± 7.7
41.9	111.0 ± 3.9
73.3	86.5 ± 6.3
122.5	84.6 ± 3.0
2397 (drop cast Silastic™ 3715)	106.2 ± 2.2
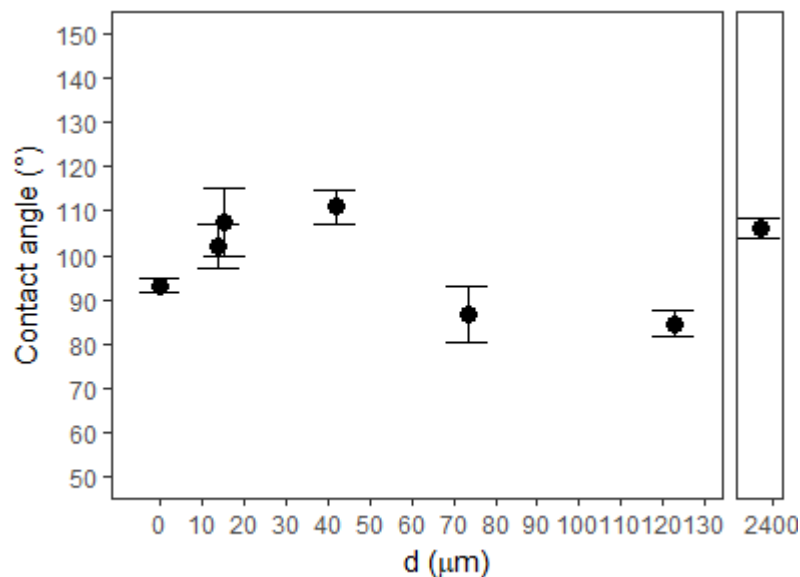
Figure 11: Contact angle as a function of topcoat thickness (d), showing no apparent correlation between them. n=6

Surface potential

One of the sources of adhesive friction is electroadhesion [30], as discussed in Chapter 2. To understand the effect of electrostatic forces present at the interface, we measured the surface potential of each sample using a Kelvin Probe. Figure 12 shows the relationship between the measured surface potential (V) and topcoat thickness (d)

for each sample (also summarized in Table 6). It appears that the V-d relationship follows a similar trend to what was observed in frictional force behavior as a function of topcoat thickness (d) which will be discussed later (see Figure 16). Thus, we hypothesize that one of the factors contributing to the variation in frictional force is the surface potential V, which would result in a change to the electroadhesive bond at the interface, as supported by Persson in a similar system where surface charge affected the real contact area (RCA) and frictional force [30]. However, we hypothesize that there must be another, more significant, contribution because the V of d=13.0μm is near the V of d=0μm (Table 6), but the frictional force of d=13.0μm is near that of d=2397μm (Table 8).

Table 6: Surface potential as a function of topcoat thickness (d). n=3

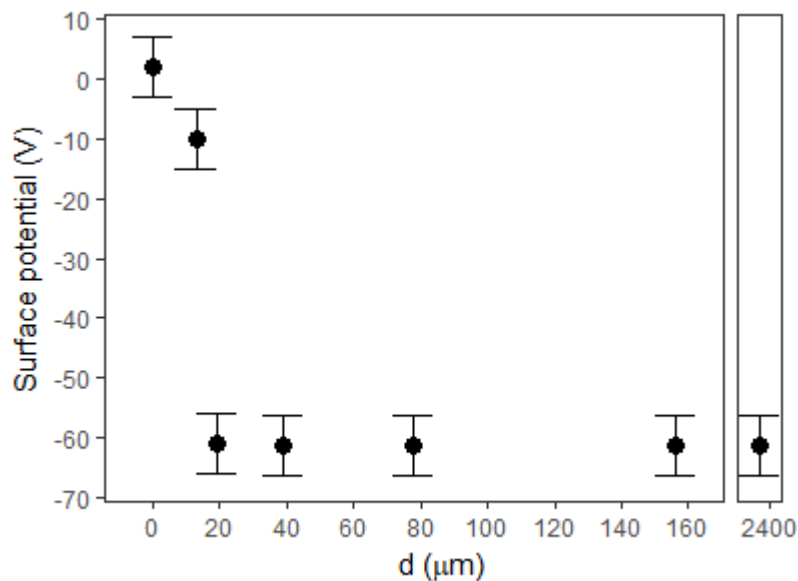| d (μm)	Surface potential (V)
0 (uncoated Sylgard® 184)	1.9 ± 5.0
13.0	-10.1 ± 5.0
19.5	-61.0 ± 5.0
39.0	-61.2 ± 5.0
78.0	-61.2 ± 5.0
156.0	-61.2 ± 5.0
2397 (drop cast Silastic™ 3715)	-61.3 ± 5.0

Figure 12: Surface potential (V) as a function of topcoat thickness (d), showing a steep drop in surface potential with d, which suggests complete coverage of samples for d > 13.0μm. n=3

Analysis of frictional force behavior

The study of frictional force was completed in three stages. In the first stage, samples of Sylgard® 184 prepared with crosslinker ratios increasing from 10:0.5 to 10:3 were tested. In the second stage, samples of Sylgard® 184 with increasing topcoat thicknesses (from d=0 to d=2397μm) were tested. Finally, in the last stage, samples of Sylgard® 184 with increasing topcoat thicknesses were immersed in LN_2 for 12 consecutive hours after which they were removed from the dewar and further tested. Measurements at both room temperature and 77K were collected.
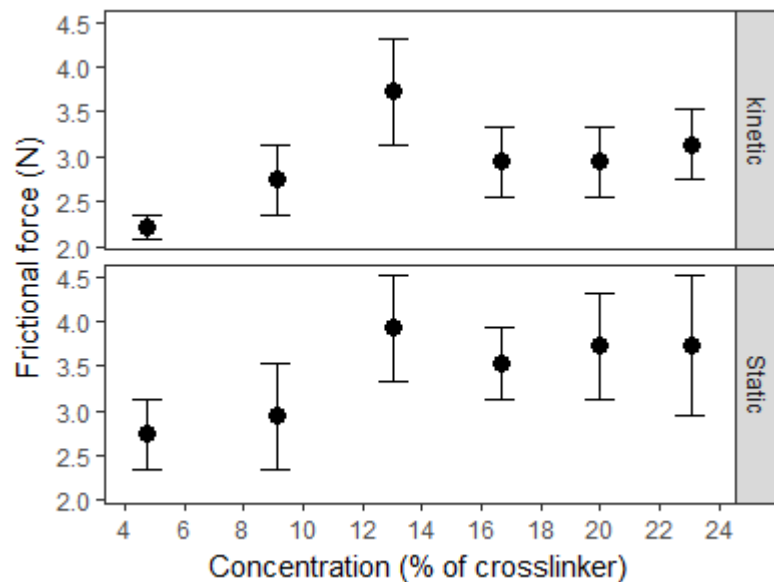
Figure 13: Frictional force as a function of crosslinker concentration, showing no apparent correlation between the two parameters. n=10

Figure 13 shows the frictional force (static and kinetic modes) of Sylgard® 184 as a function of percent crosslinker ratio. The frictional forces of the samples range from 2N to 4.5N with no apparent trend or dependency on the crosslinker ratio, which is unexpected. Given that there is a clear trend between crosslinker ratio and elastic modulus (Figure 18), and that Popov et al. [26] report a linear proportionality between frictional force and elastic modulus such that an increasing relationship between

frictional force and crosslinker concentration was initially expected. On the other hand, a strong stick-slip behavior as predicted by Gao et al. [21] was observed (Figure 15 (a)), which may be dominating the behavior and masking the effect of the elastic modulus on friction. Based on these results (Table 7, Figure 18), we decided to use 10:0.5 base prepolymer to crosslinker ratio Sylgard® 184 for other tests, since the ratio had little to no effect on the frictional force, and this ratio resulted in reproducible mechanical behavior.

Table 7: Frictional force as a function of crosslinker ratio. n=10

Ratio	Concentration (%)	Static (N)	Kinetic (N)
10:0.5	4.8	2.7 ± 0.4	2.2 ± 0.1
10:1.0	9.1	2.9 ± 0.6	2.7 ± 0.4
10:1.5	13.0	3.9 ± 0.6	3.7 ± 0.6
10:2.0	16.7	3.5 ± 0.4	2.9 ± 0.4
10:2.5	20.0	3.7 ± 0.6	2.9 ± 0.4
10:3.0	23.1	3.7 ± 0.8	3.1 ± 0.4

There is a linear relationship between the normal force and the elastic modulus (E) [26], and therefore also between the frictional force and the E [25]. The behavior of an elastic surface under load from an indenter can be modelled as a series of one-dimensional springs, each with elastic constants proportional to E, being compressed to different degrees as a function of indenter geometry, which is the basis for the Method of Dimensionality Reduction (MDR) described by Popov [26-28]. However, elastomeric friction is adhesive in nature [33, 40], which requires that the one-dimensional spring model be corrected to account for shear elongation during sliding motion. Figure 14 presents a diagram depicting the interaction of a surface polymer chain with an opposing interface to which it is adhered. As the surfaces slide in opposite directions, the chain is elongated in tension until one of the adhered ends releases, then the chain

relaxes and reattaches. This cyclic behavior is the origin of stick-slip motion in elastomers [43].
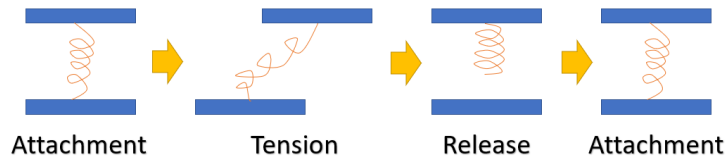

Figure 14: Diagram showcasing relationship between elasticity and friction in elastomers.

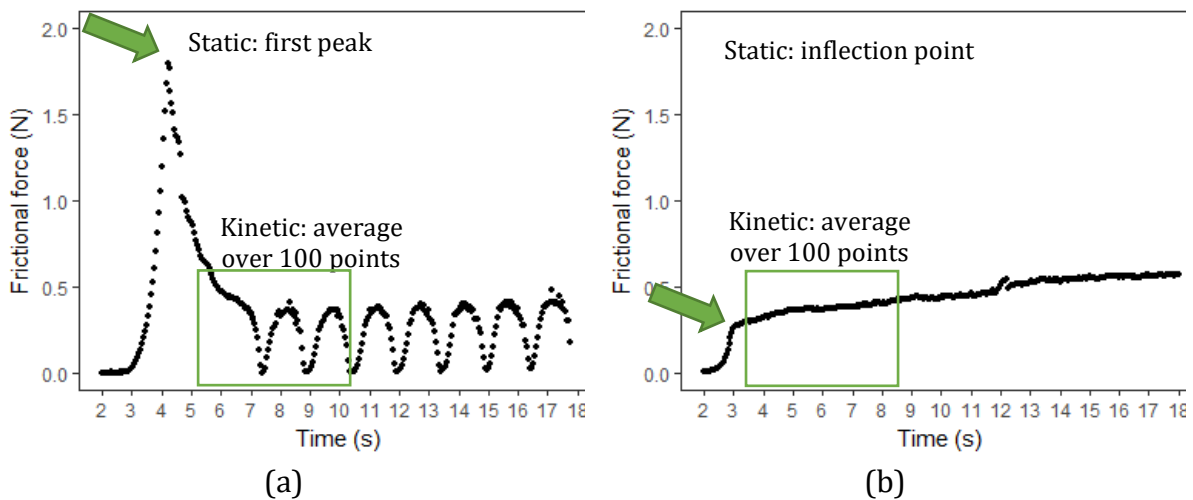(a)   (b)

Figure 15: Typical examples of frictional force over time for (a) drop cast Sylgard® 184, displaying stick-slip behavior, (b) drop cast Silastic™ 3715, showing increasing force through the experiment.

Figure 15 (a) and (b) show typical curves of frictional force over time for Sylgard® 184 and Silastic™ 3715 respectively. Highlighted with green arrows are the first peak and inflection points of the curves, which were denominated in each case the static mode of friction. Highlighted in green rectangles are a representation of the 100 points averaged to calculate the kinetic mode of friction for each case. In Figure 15 (a), the characteristic stick-slip behavior of Sylgard® 184 is prominently demonstrated, displaying one of the challenges encountered in this study. Due to stick-slip, the calculated kinetic frictional force of Sylgard® 184 is less precise than what could be achieved through nanoindentation [12, 15]. However, the values produced in this study may still be representative of what can be expected of the material in macro-scale

37

applications. Another challenge present in this study is demonstrated in Figure 15 (b), where we can observe a marked increasing slope in the kinetic portion of the friction curve. We hypothesize that this may be due to frictional heating, as PDMS is very sensitive to it [35, 51]. As a result, the longer the period over which friction is averaged, the higher the calculated value of Silastic™ 3715 kinetic friction. For this reason, the period of 5 s (100 points) was chosen for averaging, as opposed to a longer one.
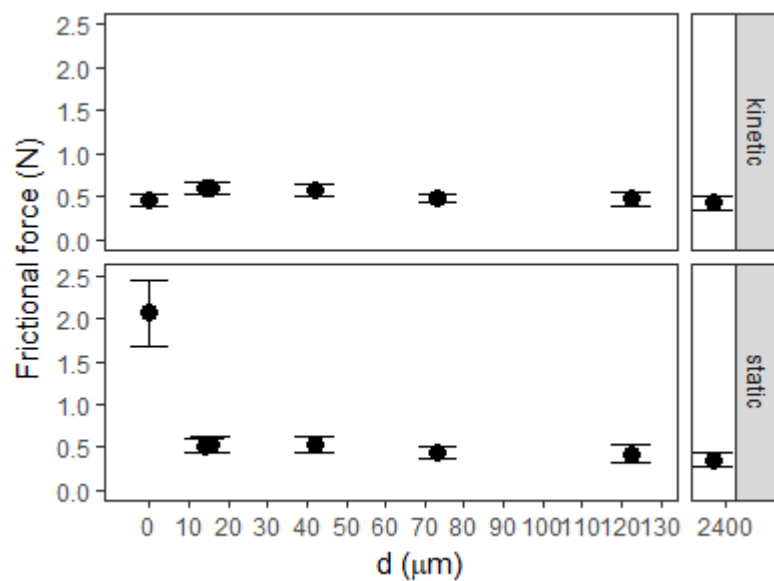

Figure 16: Frictional force as a function of topcoat thickness (d), showing complete masking for d > 0. n=10

Next the effect of topcoat thickness (d) on friction was investigated. Figure 16 shows the frictional force (static and kinetic modes) of bilayer samples as a function of topcoat thickness (d) (summarized in Table 8). For both deposition methods, regardless of topcoat thickness, the frictional forces of all bilayer samples were approximately 0.5N, a four-fold reduction in comparison to the uncoated sample of Sylgard® 184. This suggest that even for the thinnest topcoat layer reduction in friction was significant and as effective as the thicker coatings. This outcome makes Silastic™ 3715 topcoat an effective and practical method for controlling friction and degree of soiling while also allowing optical access to the Sylgard® 184 layer underneath.

38

Table 8: Frictional force as a function of topcoat thickness. n=10

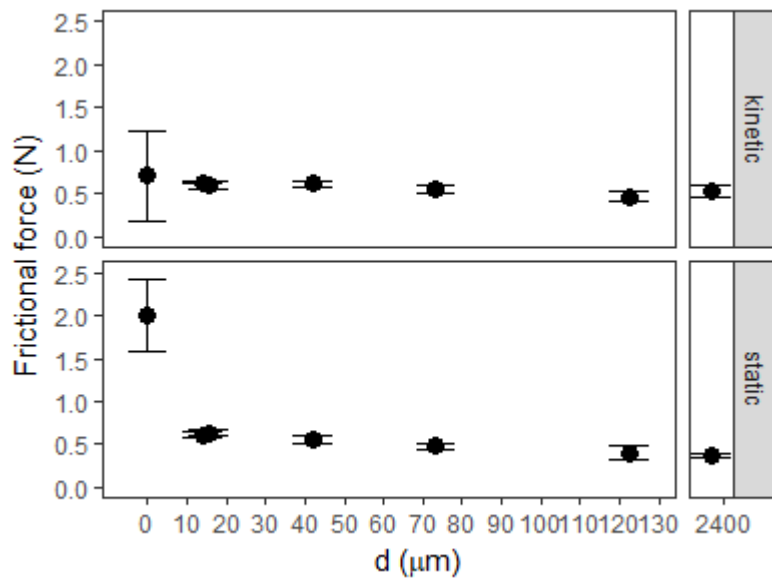| d (µm)	Static (N)	Kinetic (N)
0 (uncoated Sylgard® 184)	2.06 ± 0.39	0.45 ± 0.07
14.0	0.52 ± 0.08	0.59 ± 0.07
15.5	0.53 ± 0.08	0.59 ± 0.07
41.9	0.53 ± 0.09	0.57 ± 0.07
73.3	0.44 ± 0.08	0.47 ± 0.05
122.5	0.43 ± 0.10	0.47 ± 0.07
2397 (drop cast Silastic™ 3715)	0.35 ± 0.08	0.42 ± 0.08

Figure 17: Frictional force as a function of topcoat thickness (d) after exposure to cryogenic temperature, showing complete masking for d > 0. n=3

Figure 17 shows the frictional force (static and kinetic modes) of bilayer samples after they were immersed in liquid nitrogen for a period of 12h (summarized in Table 9) This experiment was performed in order to evaluate the integrity of the bilayer system, as well as any changes to the frictional force at lower temperatures, relevant to aerospace applications. No significant change in the frictional force was observed. We hypothesize that the interface may have rapidly returned to the same temperature that it reached during room temperature tests due to the high sensitivity of PDMS to frictional heating [35, 41], because we were limited in our ability to maintain the cryogenic temperature during testing with the equipment available. The integrity of the interface between the two materials will be discussed in subsequent sections.

Table 9: Frictional force as a function of topcoat thickness after immersion in LN_2. n=3

d (μm)	Static (N)	Kinetic (N)
0 (uncoated Sylgard® 184)	2.00 ± 0.43	0.70 ± 0.52
14.0	0.61 ± 0.04	0.63 ± 0.01
15.5	0.63 ± 0.04	0.59 ± 0.05
41.9	0.56 ± 0.05	0.62 ± 0.04
73.3	0.48 ± 0.03	0.55 ± 0.04
122.5	0.40 ± 0.08	0.46 ± 0.06
2397 (drop cast Silastic™ 3715)	0.37 ± 0.02	0.52 ± 0.07

Elastic modulus

The elastic modulus was also measured in stages; first as a function of crosslinker ratio, then as a function of topcoat thickness.
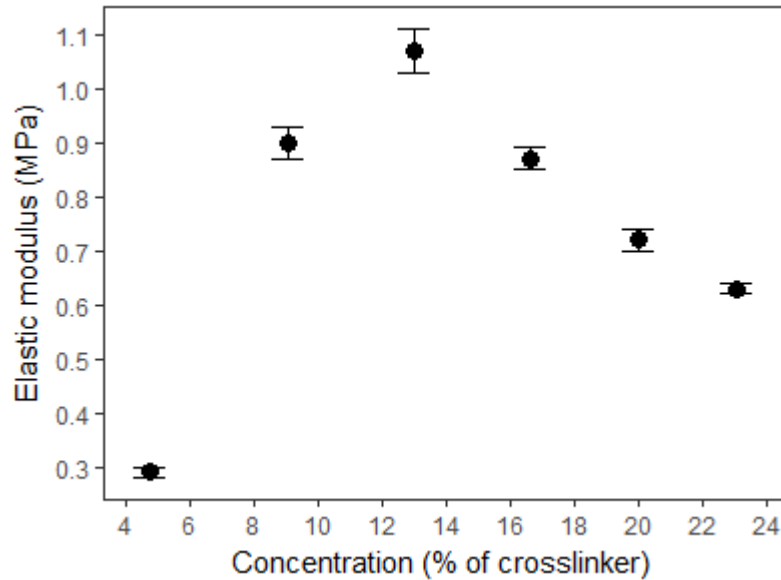

Figure 18: Tensile elastic modulus as a function of crosslinker ratio, showing an increase in E for crosslinker ratios below 10:2. n=10

Figure 18 shows the elastic modulus (in tension) of Sylgard® 184 as a function of crosslinker ratio (summarized in Table 10). It appears to peak at a ratio of 10:1.5. According to published literature, the elastic modulus in this case should continue to increase with crosslinker ratio [12] which is the trend observed in our experiments between 10:0.5 and 10:1.5. However, for values above 10:1.5, a drop in value was observed. This is still under investigation and not fully understood.

Table 10: Tensile elastic modulus as a function of crosslinker ratio. n=10

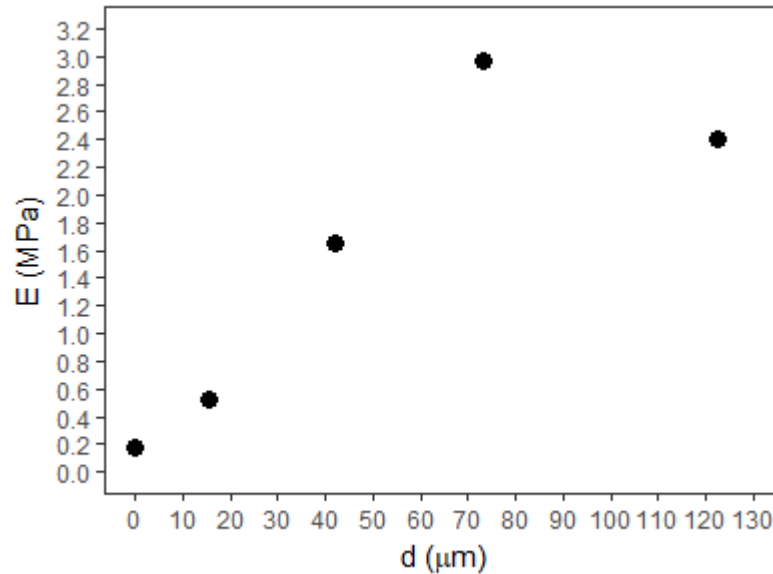| Ratio	Concentration (%)	E (MPa)
10:0.5	4.8	0.29 ± 0.01
10:1.0	9.1	0.90 ± 0.03
10:1.5	13.0	1.07 ± 0.04
10:2.0	16.7	0.87 ± 0.02
10:2.5	20.0	0.72 ± 0.02
10:3.0	23.1	0.63 ± 0.01

Figure 19: Tensile elastic modulus as a function of topcoat thickness (d), showing an increase in E with d up until the point where the bilayer material has become too brittle. n=1

Figure 19 shows the elastic modulus of the bilayer samples as a function of topcoat thickness (summarized in Table 11). It was not possible to cut a dog bone of the drop cast deposited sample, as the topcoat was too brittle and fractured, detaching from the substrate. Unfortunately, it was only possible to make enough samples for one dog bone of each sample type, which fractured on the first trial of the spin coated samples, and none for d=14.0µm due to limitations of the spin coating system. We can observe the rise in bilayer elastic modulus due to the higher E of Silastic™ 3715 (Figure 20) up until the material becomes too brittle.
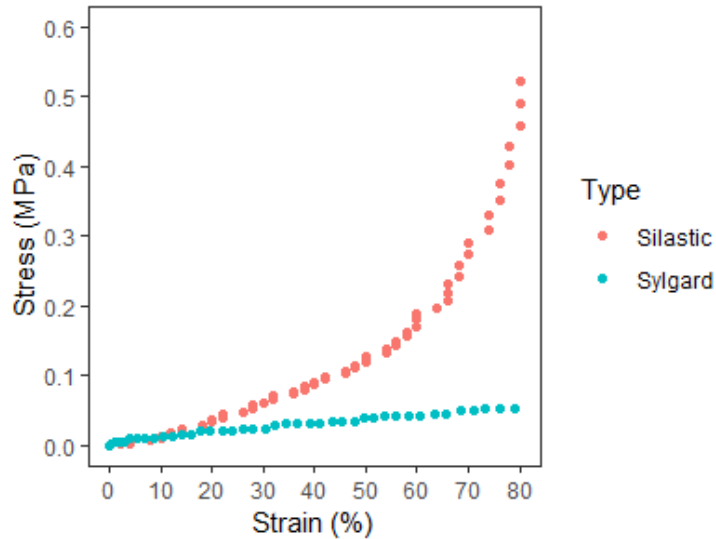
41

Figure 20: Silastic™ compression and Sylgard® tension stress-strain curves, showing the higher elastic modulus of Silastic.

Table 11: Tensile elastic modulus as a function of topcoat thickness. n=1

d (μm)	E (MPa)
0 (uncoated Sylgard® 184)	0.18
14.0	n/a
15.5	2.41
41.9	2.97
73.3	1.65
122.5	0.52
2397 (drop cast Silastic™ 3715)	n/a

Fatigue cycling

To understand the effect of strain on the bilayer material, samples were exposed to 20% strain cycles (n_c) up to 850 times, then imaged with an optical microscope (images are presented in Figure 21 with cracks and delaminated fragments highlighted in green). We observed the appearance of surface cracks even at n_c=1, and they increase in number with more cycles. There was a large variation between number of cracks from one area to another within the same sample, but samples that had been subjected to a greater number of cycles had more cracks overall than those subjected to fewer cycles. The same was true regarding number of delaminated fragments.

42
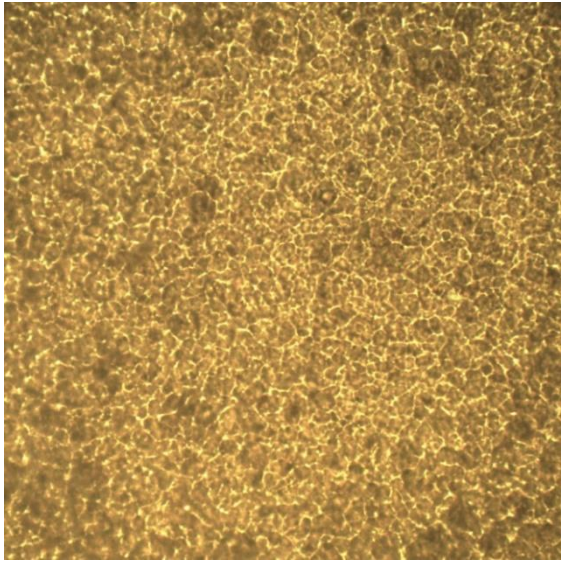
(a)
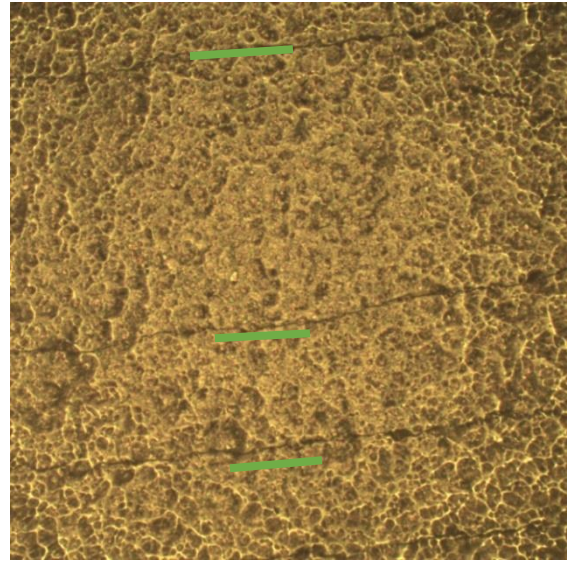
(b)
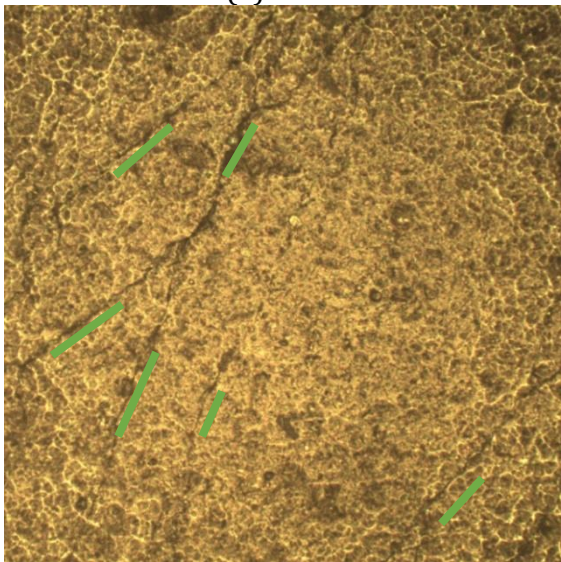
(c)

(d)

(e)

(f)

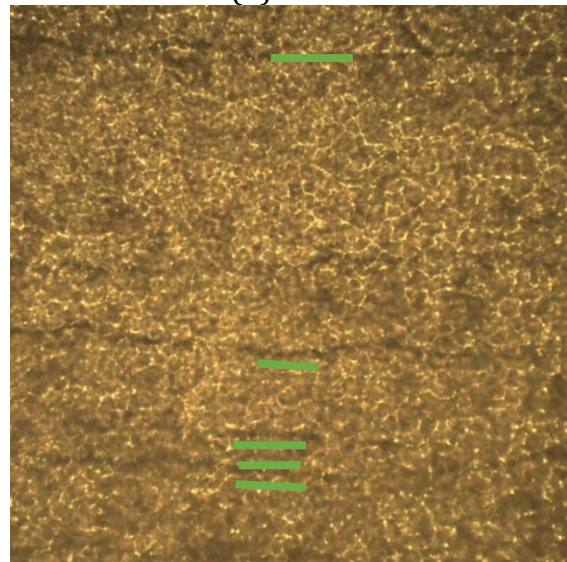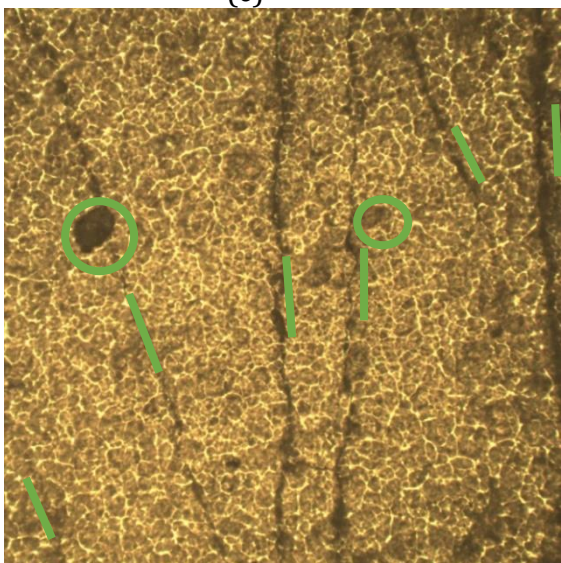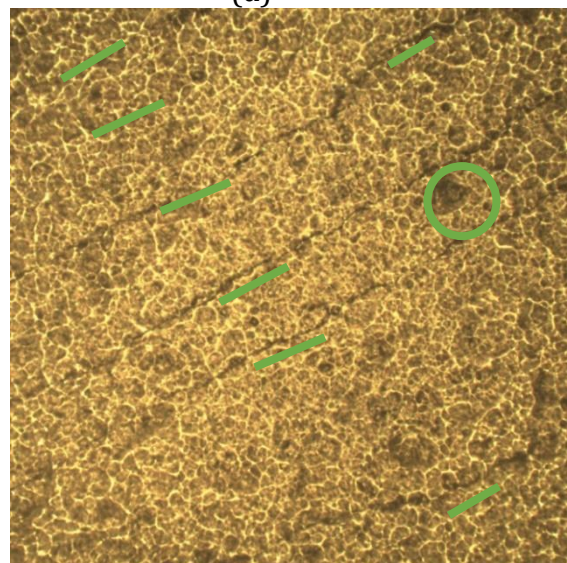Figure 21: 6.00K rpm spin coated sample after fatigue cycling, (a) n_c=0, (b) n_c=1, (c) n_c=10, (d) n_c=100, (e) n_c=300, (f) n_c=850, highlighting the increase in cracks and delamination fragments with number of cycles.

Peel strength

Peel strength was measured in two stages as well. In the first stage, samples of Sylgard® 184 prepared with different crosslinker ratios were cured between strips of aluminum foil and then the strips were pulled apart at 180°, measuring the bond of Sylgard® 184 to itself. In the second stage, a drop cast layer of Silastic™ 3715 was cured onto a layer of Sylgard® 184, then peeled at 180°, measuring the bond at the Sylgard® 184-Silastic™ 3715 interface.
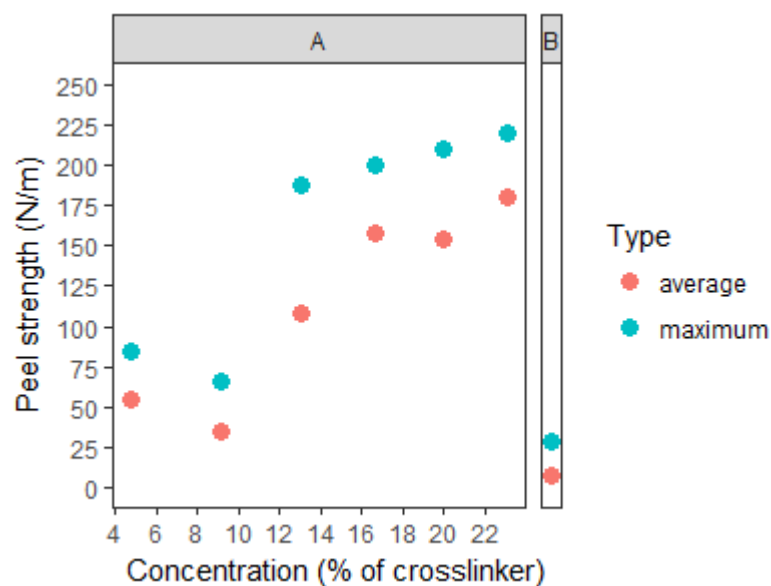
Figure 22: Peel strength (A) Sylgard® 184-Sylgard® 184 as a function of crosslinker concentration, (B) Sylgard® 184-Silastic™ 3715, showing the relative weakness of Sylgard® 184-Silastic™ 3715 bond compared to Sylgard® 184-Sylgard® 184. n=1

Figure 22 (A) shows the maximum and average 180° peel strength of the first stage, while Figure 22 (B) shows the maximum and average 180° peel strength of the second stage. Results are presented in Table 12. The strength of the bond between drop cast Silastic™ 3715 and Sylgard® 184 was significantly weaker than the internal bond of Sylgard® 184 (as expected), although an investigation with the optical microscope

revealed that patches of Silastic™ 3715 were left still bonded to Sylgard® 184 after peeling. Improving the adhesion strength will be one of the recommendations for future work.

Table 12: Peel strength by sample type. n=1

Type	Maximum (N/m)	Average (N/m)
10:0.5	84.75	54.45
10:1.0	65.75	35.27
10:1.5	187.63	107.61
10:2.0	199.63	158.26
10:2.5	210.25	154.55
10:3.0	220.25	179.50
Syl.-Sil.	28.60	7.70

UV-Vis spectroscopy

One of the most desirable properties of Sylgard® 184 is its transparency in the visible range. A well-designed topcoat layer should have none or minimal adverse impact on the desirable properties (transparency, flexibility, hydrophobicity) while circumventing the undesired properties (high friction, heavy fouling). Figure 23 (a), (b), and (c) show the percentage of transmission, reflection, and scatter, respectively, for each sample type as a function of wavelength 200nm $<\lambda<$ 800nm. Uncoated Sylgard® 184 (d=0) transmits nearly 100% in the visible range while drop cast Silastic™ 3715 (d=2397 μm) transmits nothing and reflects approximately 70%. Spin coated Silastic™ 3715 transmits up to 25% for the thinnest topcoat produced, reflects between 20% and 40%, and scatters around 75% of incident light. These results indicate that topcoat layers created at sufficiently high spin coating speeds are thin enough to allow at least 20% of the incident light to be transmitted to L1, Sylgard® 184.
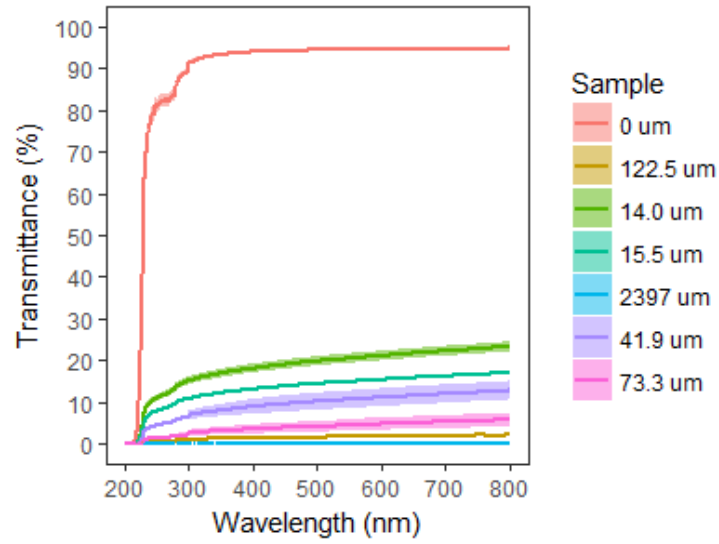
(a)
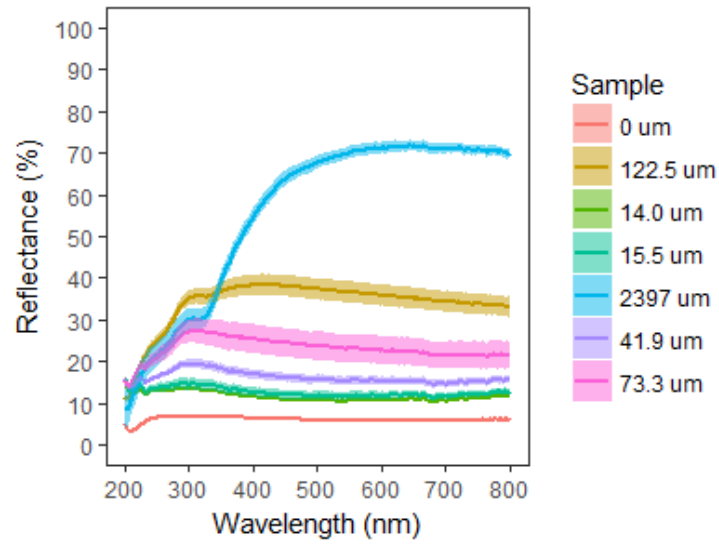
(b)
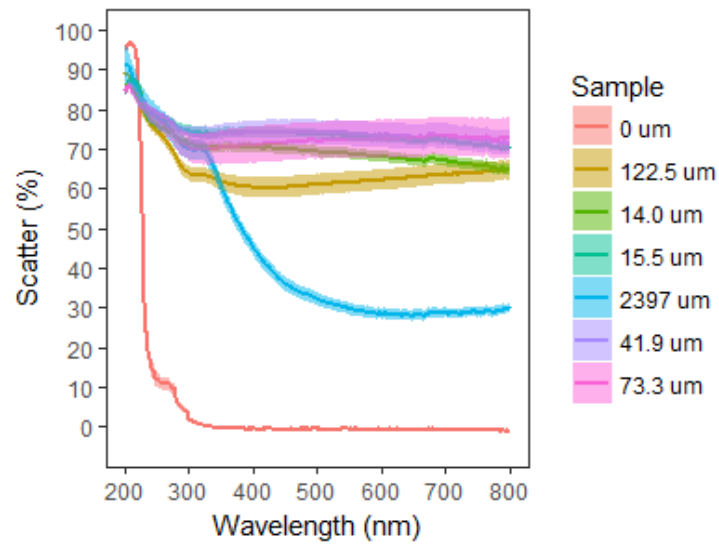
(c)

Figure 23: (a) Transmittance, (b) reflectance, (c) scatter as a function of wavelength and topcoat thickness (d), showing that d = 14.0 allows approximately 20% transmission. n=3

Phosphor thermometry

In order to demonstrate the feasibility of the topcoat layer investigated in this study for actual Sylgard® 184 applications, the temperature sensors prepared by Parajuli and Aryal [52, 53] were synthesized, coated, and tested at three separate temperatures. Sensors were coated with different thicknesses of topcoat ranging from d=0 to d=73.3μm and subject to phosphor thermometry measurements at different temperatures. In summary, results show that even for the thickest topcoat layer tested (ω=1.01K rpm, d=73.3μm) enough of the incident beam (excitation) and the emitted signal (luminescence) can travel through the topcoat layer that an accurate temperature reading is possible. Figure 24 presents the emission curve for each sample, while Figure 25 presents emission curves as a function of temperature, showing little dependence on coating thicknesses (d). This data was used to calculate decay times and are presented in Table 13.

In-depth phosphor thermometry is beyond the scope of this study but, given the encouraging results of the previous section, the following measurements were made as a proof of concept, to determine whether enough luminescence could be transmitted through the topcoat to detect.

Table 13: Calculated decay time. n=1

Platform Temperature (°C)	Decay time (ms)
100	3.15 ± 0.03
25	3.76 ± 0.07
-50	4.41 ± 0.05
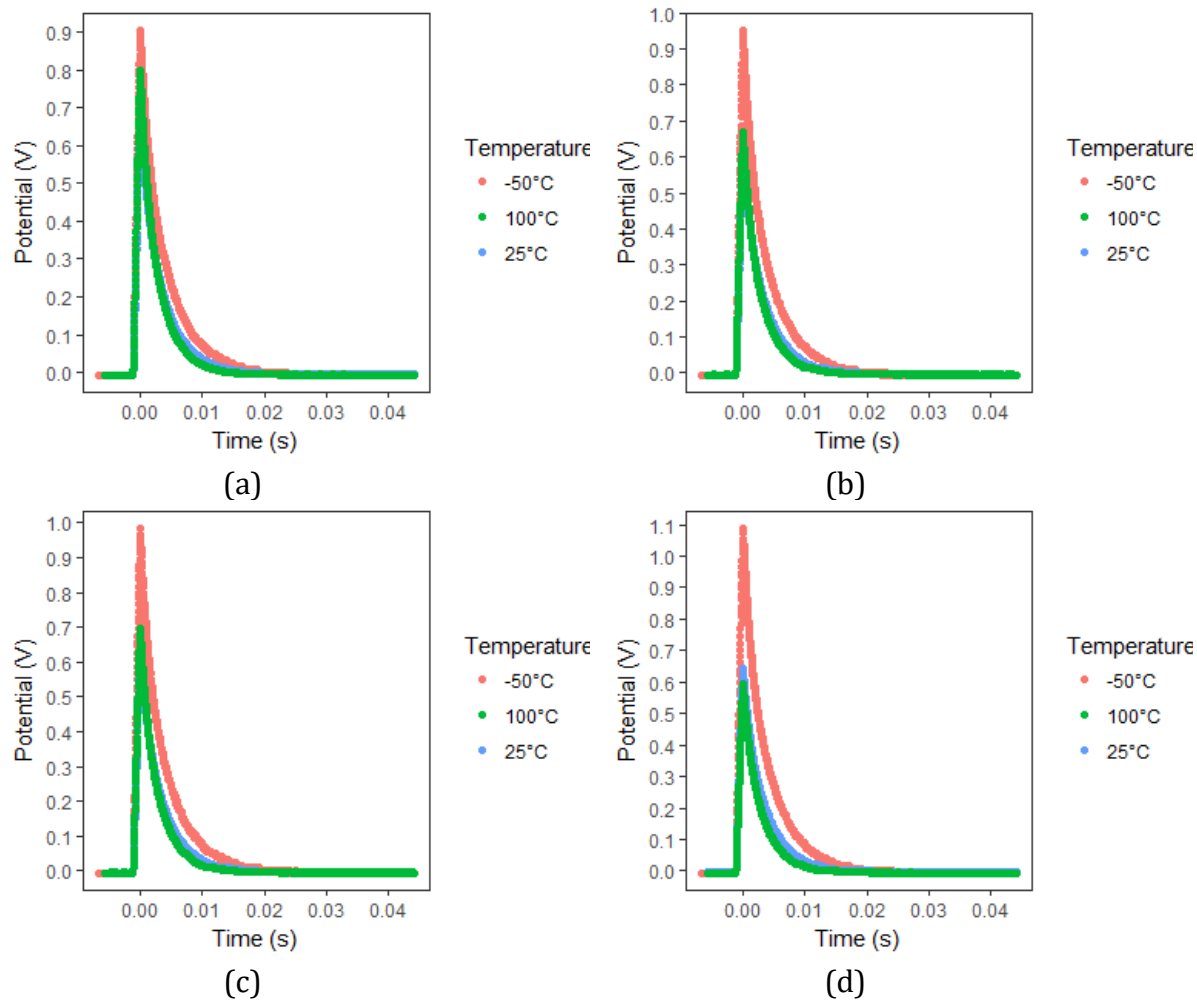
Figure 24: Luminescence of all temperatures for (a) uncoated sample, (b) 4.02K rpm spin coated sample, (c) 2.01K rpm spin coated sample, and (d) 1.01K rpm spin coated sample, showing that all sample types permitted emission detection. n=1
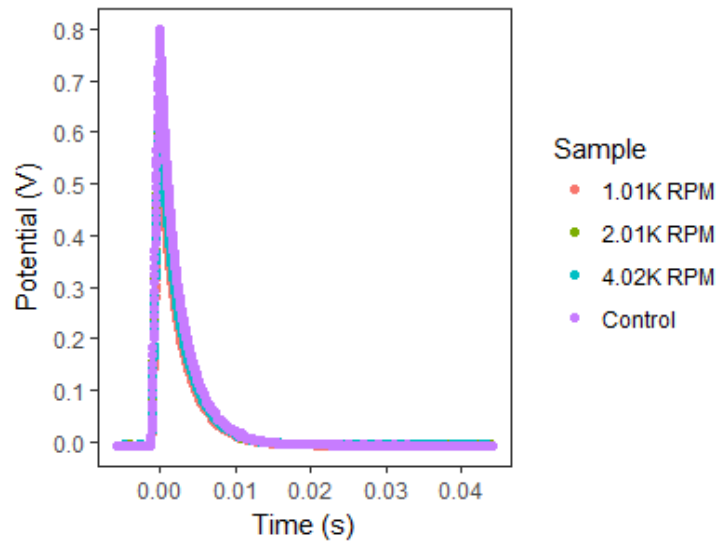
(a)
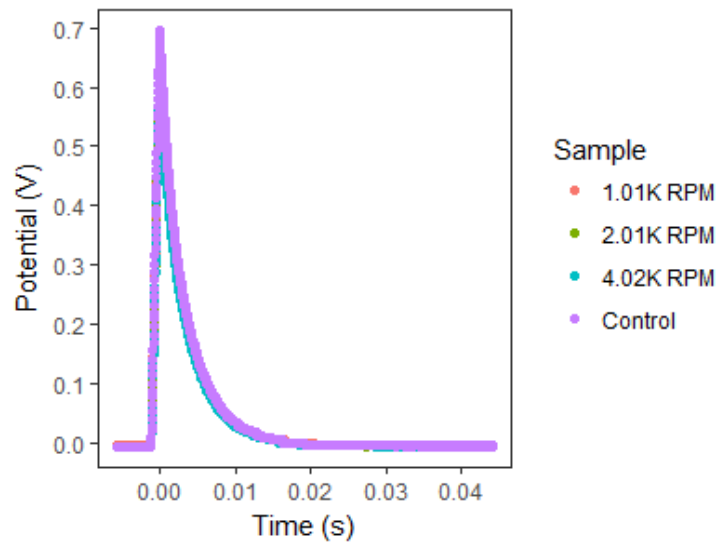
(b)
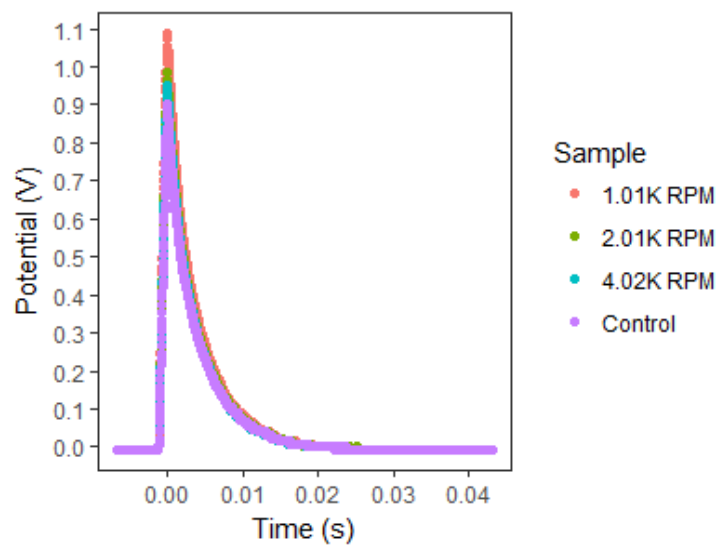
(c)

Figure 25: Luminescence for all samples for (a) 100°C, (b) 25°C, (c) -50°C, showing that topcoat thickness didn't change the characteristic curve for each temperature. n=1

Summary

First, the elastic behavior of Sylgard® 184 was measured as a function of crosslinker ratio, enabling the most appropriate choice for the planned bilayer substrate. Then, different deposition methods were attempted to determine which would generate best bilayer integrity. We were able to control the topcoat thickness by regulating the angular speed during the spin coating process.

We demonstrated that spin coating with Silastic™ 3715 can successfully reduce the frictional force of Sylgard® 184 by approximately a factor of 4 regardless of coating thickness and exposure to cryogenic temperature and showed the feasibility of using this bilayer structure for phosphor thermometry.

Finally, we investigated several surface and bulk properties of the bilayer to deduce the principal source of the variation in frictional force.

5. Conclusion and future recommendations

The goal of this study was to investigate methods to control the coefficient of friction of Sylgard® 184 PDMS. The approach taken was to create thin uniform topcoats of another material on top of the Sylgard® 184 and then characterize the surface and bulk properties of the bilayer in order to understand the properties of the new material. The material chosen as the topcoat layer was Silastic™ 3715 and was deposited in two different ways.

During this study we confirmed that the mechanical properties of Sylgard® 184 are highly dependent on the crosslinker ratio and the curing temperature. This work has shown that there is a peak elastic modulus to be attained by adjusting the crosslinker ratio while keeping the curing time and temperature fixed to values reported in Chapter 4.

We have also demonstrated that it is possible to create thin continuous and homogeneous films of Silastic™ 3715 on Sylgard® 184 by means of spin coating technique. The presence of the topcoat Silastic™ 3715 layer proved to be an effective method to reduce Sylgard® 184 frictional force by at least a factor of four but resulted in an increase in elastic modulus by a factor between 2 and 16, depending on topcoat thickness, and reduction in fracture strain, due to the formation of surface cracks. The bilayer demonstrated tolerance to thermal cycling and being exposed to extreme temperatures and showed no signs of delamination or peeling.

The profilometry showed little change in the surface roughness between uncoated Sylgard® 184, spin coated Silastic™ 3715 on Sylgard® 184 and drop cast Silastic™ 3715 on Sylgard® 184. Therefore, we hypothesize that the reduction in friction is not attributed to an alteration of the surface roughness. This was unexpected, given the

Murarash et al. study showing a strong correlation between frictional force and surface texturing on polymers [16], but this wasn't the case here.

One possible explanation for the reduction in frictional force is in the difference in elastic modulus between Sylgard® 184 and Silastic™ 3715. The elastic modulus of Sylgard® 184 is significantly lower than that of Silastic™ 3715. This means that, when pressed against a counterface by equal loads, the asperities of a Sylgard® 184 surface will deform more than those of a Silastic™ 3715 surface. Figure 26 shows a diagram of the model. Given two hemispherically modeled asperity peaks of identical geometry but substantially different elasticity, the material with lower elastic modulus (E) will result in a greater real contact area (RCA) than that of the higher elastic modulus. This change in RCA would result in a lower frictional force [21, 35].
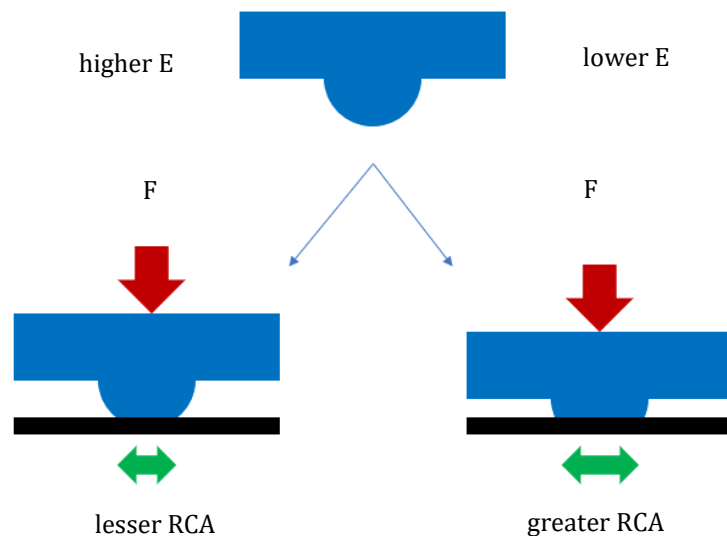
Figure 26: Identical asperities resulting in different real contact area (RCA) due to differing elastic moduli (E).

The spin coated bilayer allowed enough transmission to perform phosphor thermometry, even at the lowest rotation speed tested.

Future recommendations

Future studies of this material could be done to improve and optimize many of the characterization techniques. The apparatus used to perform low temperature friction tests was rudimentary and couldn't maintain a fixed temperature distinct from room temperature. Similarly, high temperature friction testing protocols must be developed. Some tests couldn't be performed with samples spin coated at high speed (higher than 4K rpm) due to limitations of the fabrication equipment.

Another possible avenue of investigation would be to more accurately determine the bilayer's friction components; load-dependent and area-dependent; as well as the effect of sliding speed and other interface materials. Also, more work could be done to quantify the material's fatigue wear rate as a function of maximum strain and topcoat thickness.

References

[1]   Babak Ziaie, Antonio Baldi, Ming Lei, Yuandong Gu, and Ronald A. Siegel. Hard and soft micromachining for biomems: review of techniques and examples of applications in microfluidics and drug delivery. *Advanced drug delivery reviews*, 56(2):145–172, 2004.

[2]   Farhang Abbasi, Hamid Mirzadeh, and Ali-Asgar Katbab. Modification of polysiloxane polymers for biomedical applications: a review. *Polymer International*, 50(12):1279–1287, 2001.

[3]   James Njuguna and Krzysztof Pielichowski. Polymer nanocomposites for aerospace applications: properties. *Advanced Engineering Materials*, 5(11):769–778, 2003.

[4]   Morteza Amjadi, Ki-Uk Kyung, Inkyu Park, and Metin Sitti. Stretchable, skin-mountable, and wearable strain sensors and their potential applications: a review. *Advanced Functional Materials*, 26(11):1678–1698, 2016.

[5]   Ilker Murat Koç and Emre Akça. Design of a piezoelectric based tactile sensor with bio-inspired micro/nano-pillars. *Tribology International*, 59:321–331, 2013.

[6]   Pratikshya Parajuli, Stephen W Allison, and Firouzeh Sabri. Spin coat fabricated multilayer pdms-phosphor composites for thermometry. *Measurement Science and Technology*, 28(6):065101, 2017.

[7]   Dow Corning. Sylgard® 184 Silicone Elastomer. `goo.gl/EVuSSF`, 2018. [Online; accessed 11-May-2018].

[8]   Brian J Kirby and Ernest F Hasselbrink. Zeta potential of microfluidic substrates: 2. data for polymers. *Electrophoresis*, 25(2):203–213, 2004.

[9]   Emanuel A Waddell, Stephen Shreeves, Holly Carrell, Christopher Perry, Branden A Reid, and James McKee. Surface modification of Sylgard® 184 polydimethylsiloxane by 254 nm excimer radiation and characterization by contact

angle goniometry, infrared spectroscopy, atomic force and scanning electron microscopy. *Applied Surface Science*, 254(17):5314–5318, 2008.

[10] Ross S Fontenot, Stephen W Allison, Kyle J Lynch, William A Hollerman, and Firouzeh Sabri. Mechanical, spectral, and luminescence properties of ZnS: Mn doped pdms. *Journal of Luminescence*, 170:194–199, 2016.

[11] ID Johnston, DK McCluskey, CKL Tan, and MC Tracey. Mechanical characterization of bulk Sylgard® 184 for microfluidics and microengineering.
Journal of Micromechanics and Microengineering, 24(3):035017, 2014.

[12] Fernando Carrillo, Shikha Gupta, Mehdi Balooch, Sally J Marshall, Grayson W Marshall, Lisa Pruitt, and Christian M Puttlitz. Nanoindentation of polydimethylsiloxane elastomers: Effect of crosslinking, work of adhesion, and fluid environment on elastic modulus. *Journal of materials research*, 20(10):2820–2830, 2005.

[13] Dhananjay Bodas, Jean-Yves Rauch, and Chantal Khan-Malek. Surface modification and aging studies of addition-curing silicone rubbers by oxygen plasma. *European Polymer Journal*, 44(7):2130-2139, 2008.

[14] David T Eddington, John P Puccinelli, and David J Beebe. Thermal aging and reduced hydrophobic recovery of polydimethylsiloxane. *Sensors and Actuators B: Chemical*, 114(1):170–172, 2006.

[15] Bo He, Wei Chen, and Q Jane Wang. Surface texture effect on friction of a microtextured poly (dimethylsiloxane)(pdms). *Tribology Letters*, 31(3):187, 2008.

[16] Boris Murarash, Yan Itovich, and Michael Varenberg. Tuning elastomer friction by hexagonal surface patterning. *Soft Matter*, 7(12):5553–5557, 2011.

[17] Leonid Gitlin, Philipp Schulze, Stefan Ohla, Hans-Josef Bongard, and Detlev Belder. Surface modification of pdms microfluidic devices by controlled sulfuric acid

treatment and the application in chip electrophoresis. *Electrophoresis*, 36(3):449-56, 2015.

[18] Marc-Antoine Campeau, Audrey Lortie, Pierrick Tremblay, Marc-Olivier Béliveau, Dominic Dubé, Eve Langelier, and Léonie Rouleau. Effect of manufacturing and experimental conditions on the mechanical and surface properties of silicone elastomer scaffolds used in endothelial mechanobiological studies. *Biomedical engineering online*, 16(1):90, 2017.

[19] T Baumberger, C Caroli, B Perrin, and O Ronsin. Nonlinear analysis of the stick-slip bifurcation in the creep-controlled regime of dry friction. *Physical Review E*, 51(5):4005, 1995.

[20] JX Dong, ZS Hu, and GX Chen. Preparation and tribology of aerogel silica and alumina-silica as lubricant oil additives. *Lubrication Science*, 11(3):285–295, 1999.

[21] Jianping Gao, WD Luedtke, D Gourdon, M Ruths, JN Israelachvili, and Uzi Landman. Frictional forces and Amontons' law: from the molecular to the macroscopic scale, 2004.

[22] Qing Zhang, Yue Qi, Louis G Hector Jr, Tahir Cagin, and William A. Goddard III. Origin of static friction and its relationship to adhesion at the atomic scale. *Physical Review B*, 75(14):144114, 2007.

[23] Karthika Mohan. Frictional analysis of aerospace alloys and composite materials. *The School of Mechanical and Manufacturing Engineering, University of New South Wales, Sydney*, 2011.

[24] AG Mamalis and AK Vortselas. Wear of ceramic interfaces: Multiscale statistical simulation. *Wear*, 294:402–408, 2012.

[25] Aljaž Pogačnik and Mitjan Kalin. How to determine the number of asperity peaks, their radii and their heights for engineering surfaces: A critical appraisal. *Wear*, 300(1-2):143–154, 2013.

[26] Valentin L Popov. Method of reduction of dimensionality in contact and friction mechanics: A linkage between micro and macro scales. *Friction*, 1(1):41–62, 2013.

[27] VL Popov. Method of dimensionality reduction in contact mechanics and tribology. heterogeneous media. *Physical Mesomechanics*, 17(1):50–57, 2014.

[28] Valentin L Popov and Markus Heß. Method of dimensionality reduction in contact mechanics and friction. *Springer*, 2015.

[29] Christian Greiner, Zhilong Liu, Reinhard Schneider, Lars Pastewka, and Peter Gumbsch. The origin of surface microstructure evolution in sliding friction. *Scripta Materialia*, 153:63–67, 2018.

[30] BNJ Persson. The dependency of adhesion and friction on electrostatic attraction. *The Journal of chemical physics*, 148(14):144701, 2018.

[31] KA Grosch. The relation between the friction and visco-elastic properties of rubber. *Proc. R. Soc. Lond. A*, 274(1356):21–39, 1963.

[32] JK Lancaster. Relationships between the wear of polymers and their mechanical properties. In *Proceedings of the Institution of Mechanical Engineers, Conference Proceedings*, volume 183, pages 98–106. SAGE Publications Sage UK: London, England, 1968.

[33] Yu B Chernyak and AI Leonov. On the theory of adhesive friction of elastomers. *Annals of the New York Academy of Sciences*, 452(1):129–145, 1985.

[34] Jaydeep Khedkar, Ioan Negulescu, and Efstathios I Meletis. Sliding wear behavior of ptfe composites. *Wear*, 252(5-6):361–369, 2002.

[35] NK Myshkin, MI Petrokovets, and AV Kovalev. Tribology of polymers: adhesion, friction, wear, and mass-transfer. *Tribology International*, 38(11-12):910–921, 2005.

[36] Q Li, M Popov, A Dimaki, AE Filippov, S Kürschner, and VL Popov. Friction between a viscoelastic body and a rigid surface with random self-affine roughness. *Physical review letters*, 111(3):034301, 2013.

[37] Qiang Li, Andrey Dimaki, Mikhail Popov, Sergey G Psakhie, and Valentin L Popov. Kinetics of the coefficient of friction of elastomers. *Scientific reports*, 4:5795, 2014.

[38] Lars Voll. Experimental investigation of the adhesive contact with elastomers: Effect of surface roughness. *Facta Universitatis, Series: Mechanical Engineering*, 13(1):33–38, 2015.

[39] L Chang, K Friedrich, and G Zhang. New insights into wear behavior of high-performance polymers. In *Proceedings of the 14th IFToMM World Congress*, pages 688–694, 2015.

[40] Mohammad Al-Assi and Emad Kassem. Evaluation of adhesion and hysteresis friction of rubber–pavement system. *Applied Sciences*, 7(10):1029, 2017.

[41] A Tiwari, N Miyashita, N Espallargas, and BNJ Persson. Rubber friction: The contribution from the area of real contact. *The Journal of chemical physics*, 148(22):224701, 2018.

[42] Katherine Vorvolakos and Manoj K Chaudhury. The effects of molecular weight and temperature on the kinetic friction of silicone rubbers. *Langmuir,* 19(17):6778–6787, 2003.

[43] Lucas Landherr. Investigation of the interfacial friction and adhesion of thin pdms network lubricant films. 2010.

[44] Gael Pallares, Riad Sahli, Imed Ben Ali, Samer Al Akhrass, and Julien Scheibert. Effect of coating thickness on the friction properties of rubber-sphere on rubber-coated-plane contacts. *S19 Tribologie et mécanique du contact*, 2015.

[45] Dow Corning. Silastic™ 3715 Topcoat. `goo.gl/n9qDKw`, 2018. [Online; accessed 11-May-2018].

[46] S Timoshenko and JN Goodier. Theory of elasticity. 1951. *New York*, 412:108.

[47] James Ward. Young's modulus. *Encyclopedia britannica*, 1886.

[48] Rudiger Paschotta. Rp photonics encyclopedia. *RP Photonics*, 26(06), 2013.

[49] Biotronix. Optical densities in biotechnology. `https://goo.gl/AfXbPh`, 2018. [Online; accessed 13-Aug-2018].

[50] Yuehua Yuan and T Randall Lee. Contact angle and wetting properties. In *Surface science techniques*, pages 3–34. Springer, 2013.

[51] Junji Sakamoto, Yong-Sung Lee, and Seong-Kyun Cheong. Effect of surface flaw on fatigue strength of shot-peened medium-carbon steel. *Engineering Fracture Mechanics*, 133:99-111, 2015.

[52] Pratikshya Parajuli. *Exploration of thin film polymers for phosphor thermometry*. Master thesis, University of Memphis, 2017.

[53] Makunda Aryal. *Heat flux calculation of PDMS and silica aerogel through phosphor thermometry*. Master thesis, University of Memphis, 2018.

[54] Elveflow. How to do a spin-coated PDMS layer? – Application Note. `https://goo.gl/6asR4F`, 2018. [Online; accessed 10-Nov-2018].

[55] Elveflow. PDMS: a review, 2018. `https://goo.gl/83WRMh`, 2018. [Online; accessed 10-Nov-2018].

[56] Sabbah, A., Youssef, A. and Damman, P., 2016. Superhydrophobic Surfaces Created by Elastic Instability of PDMS. *Applied Sciences*, 6(5), p.152.

[57] Zhang, H., & Chiao, M. (2015). Anti-fouling coatings of poly (dimethylsiloxane) devices for biological and biomedical applications. *Journal of medical and biological engineering*, *35*(2), 143-155.

[58] Polizos, G., Sharma, J. K., Smith, D. B., Tuncer, E., Park, J., Voylov, D., ... & Aman, M. (2018). Anti-soiling and highly transparent coatings with multi-scale features. *Solar Energy Materials and Solar Cells*, *188*, 255-262.

[59] Sabri, F., Leventis, N., Hoskins, J., Schuerger, A. C., Sinden-Redding, M., Britt, D., & Duran, R. A. (2011). Spectroscopic evaluation of polyurea crosslinked aerogels, as a substitute for RTV-based chromatic calibration targets for spacecraft. *Advances in Space Research*, *47*(3), 419-427.

[60] Banerjee, I., Pangule, R. C., & Kane, R. S. (2011). Antifouling coatings: recent developments in the design of surfaces that prevent fouling by proteins, bacteria, and marine organisms. *Advanced materials*, *23*(6), 690-718.

[61] Vasudevan, R., Kennedy, A. J., Merritt, M., Crocker, F. H., & Baney, R. H. (2014). Microscale patterned surfaces reduce bacterial fouling-microscopic and theoretical analysis. *Colloids and Surfaces B: Biointerfaces*, *117*, 225-232.

Appendix A Python code for calculating static and kinetic coefficient of friction

In this chapter is the custom Python application used to find static frictional force and calculate kinetic frictional force.

```python
import openpyxl

def average(startRow, col, mr):
total = 0.0
count = 0
for i in range(100):
#print ws.cell(row = startRow + i, column = col).value
if startRow + i < mr:
total += ws.cell(row = startRow + i, column = col).value
count += 1
return total / count

if __name__ == "__main__":
with open("analysis.csv", "w+") as file:
file.write("Type, Sample, Run, Static CoF, Kinetic CoF\n")

for i in range(78):
number_of_file = i + 1
name_of_file = "Book" + str(number_of_file) + ".xlsx"
print "Analyzing file " + name_of_file + " ...",
wb = openpyxl.load_workbook(filename = name_of_file)
ws = wb.active
mr = ws.max_row
#print mr
mc = ws.max_column

this_type = ws['F1'].value
#print this_type
this_sample = ws['F2'].value[1]
```

62

```
#print this_sample
this_run = ws['F3'].value[1]
#print this_run

for i in range(2, mr+1):
if ws.cell(row = i, column = 2).value > ws.cell(row = i + 1,
column = 2).value and ws.cell(row = i, column = 2).value >
0.1:
peak_index = i
#print peak_index
break

scof = ws.cell(row = peak_index, column = 2).value
#print scof

kcof = average(peak_index + 1, 2, mr)

file.write("%s, %s, %s, %s, %s\n" % (this_type, this_sample,
this_run, scof, kcof))
print "Done"
```